

Dear Topical Editor and Reviewers:

On behalf of my co-authors, we thank you very much for reviewing our manuscript and giving us a lot of useful comments and suggestions. We appreciate the comments on our manuscript entitled “GLC\_FCS30D: The first global 30-m land-cover dynamic monitoring product with a fine classification system from 1985 to 2022 using dense time-series Landsat imagery and continuous change-detection method” (essd-2023-320).

We have revised the manuscript carefully according to the comments. All the changes were highlighted (red color) in the manuscript. And the point-by-point response to the comments of the reviewers is also listed below.

Looking forward to hearing from you soon.

Best regards,

Prof. Liangyun Liu

[liuly@radi.ac.cn](mailto:liuly@radi.ac.cn)

Institute of Remote Sensing and Digital Earth, Chinese Academy of Sciences

No.9 Dengzhuang South Road, Haidian District, Beijing 100094, China

## Response to comments

**Paper #:** essd-2023-320

**Title:** GLC\_FCS30D: The first global 30-m land-cover dynamic monitoring product with a fine classification system from 1985 to 2022 using dense time-series Landsat imagery and continuous change-detection method

**Journal:** Earth System Science Data

### Reviewer #1

This paper greatly attempts to map the annual global land cover change using all Landsat observations and the CCD approach. The paper is well written with clear logic, while some issues need to be clarified for publication as a scientific data paper.

Great thanks for the positive comments. The manuscript has been greatly improved based on your and another reviewers' comments and suggestions.

1. The CCDC approach is very sensitive to the parameters adopted, which may identify pseudo changes. This may directly relate to the derived temporal stable regions, and further impact the results of global changed areas (as well as the statistics). As a scientific data paper, this part should be enhanced with quantitative analysis, especially the uncertainty of change detection across different cover types.

Great thanks for the comment. Yes, we agree that the CCDC algorithm was sensitive to the parameter settings, thus the sensitive analysis between three sensitive parameters (minObservations, chiSquareProbability and minNumOfYearScaler) with the land-cover change detection accuracy (omission error and commission error) were supplemented, and the results showed that there was a correlation between the omission error and commission error with the variability of the parameter's values.

In specific, the descriptions of sensitive analysis and how to determine the values of the sensitive parameters have been added in the Section 3.2 as:

Next, the CCD was also a multi-parameter change detection model and demonstrated to be sensitive to the parameter settings (Xiao et al., 2023; Zhu and Woodcock, 2014b). The CCDC algorithm on the Google Earth Engine platform (ee.Algorithms.TemporalSegmentation.Ccdc) contained three key adjustable parameters: minObservations, chiSquareProbability and minNumOfYearScaler. Zhu et al. (2019) analyzed the relationships between the omission error and commission error of land-cover changes with the variability of three parameters in the United States, and found their values affected the change detection accuracy. In this study, we also investigated the sensitivity between parameter settings with the change detection accuracies in Figure S1 (seen the Supplement material) using the time-series points from LCMAP\_Val and LUCAS datasets after partly sampling. Notably, the sensitivity analysis was implemented in two large-areas for ensure the feasibility of optimal parameters, that is, which will be suitable for other areas in land-cover change detection. The results also showed the CCD is a parameter-sensitive algorithm and the optimal parameter values were 5, 0.95 and 2-year for minObservations, chiSquareProbability and minNumOfYearScaler.

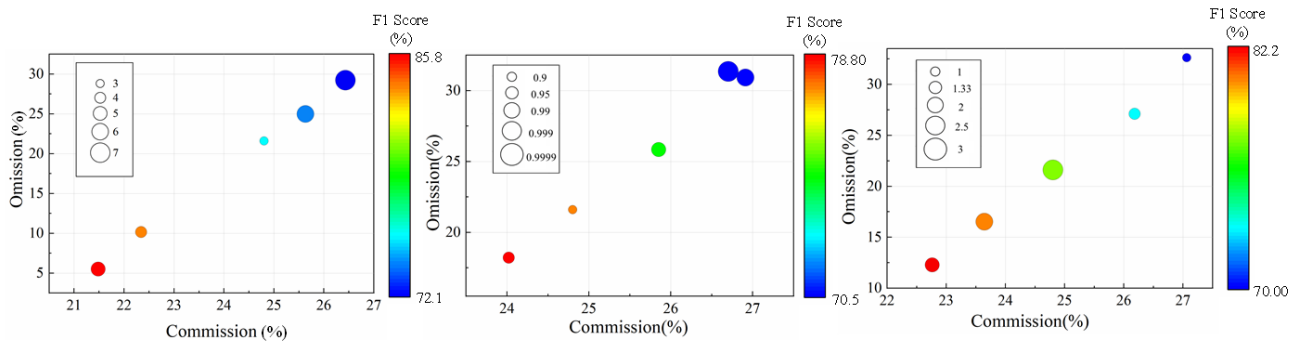


Figure S1. The sensitive analysis between the omission error and commission error with the minObservations, chiSquareProbability and minNumOfYearScaler using the time-series points from LCMAP\_Val and LUCAS datasets after partly sampling.

Xiao, Y., Wang, Q., Tong, X., and Atkinson, P. M.: Thirty-meter map of young forest age in China, *Earth Syst. Sci. Data*, 15, 3365-3386, <https://doi.org/10.5194/essd-15-3365-2023>, 2023.

Zhu, Z., Zhang, J., Yang, Z., Aljaddani, A. H., Cohen, W. B., Qiu, S., and Zhou, C.: Continuous monitoring of land disturbance based on Landsat time series, *Remote Sensing of Environment*, <https://doi.org/10.1016/j.rse.2019.03.009>, 2019.

Meanwhile, using the values were 5, 0.95 and 2 years for minObservations, chiSquareProbability and minNumOfYearScaler, we also analyzed the uncertainty of the CCD algorithm at various land-cover change types based on the random sampling land-cover changed points from NLCD products over the United States in Table S1.

Table S1. The uncertainty analysis of CCD algorithm for different land-cover change types using the random sampling land-cover changed points from NLCD products over the United States.

	To cropland	To forest	To shrubland	To grassland	To water	To bareland	To impervious surface
P.A. (±SE)	70.00(0.55)	45.64(0.49)	42.02(0.89)	66.13(0.33)	77.05(0.54)	42.86(1.32)	70.65(0.42)
U.A. (±SE)	46.10(0.48)	64.66(0.56)	23.81(0.56)	43.94(0.28)	58.02(0.55)	35.29(1.16)	57.33(0.42)

It should be noted that the wetland was independently generated, and the permanent snow ice and tundra were sparse distributed on the United States, the uncertainty analysis of CCD for these three classes were excluded.

2. As a global land cover change dataset, the accuracy assessment regarding those changed pixels should be significantly improved. The confusion matrix just shows the accuracy in 2020, while those changes in different years with field samples

Great thanks for the comment. Yes, we completely agree that the accuracy analyzing for those changed pixels should be taken care. However, collecting a time-series global validation datasets are greatly difficult and challenging, and **there is currently no public long time-series validation datasets.**

In this revision, the time-series LCMAP\_Val and LUCAS validation points are further used to calculate the accuracy metrics of changed and unchanged pixels. It should be noted that ‘changed’ and ‘unchanged’ referred to the work of Stehman et al. (2021) in validating the LCMAP annual land cover products during 1985-2017. The specific analysis about land-cover changed pixels are added as:

### Section 3.4 Accuracy assessment

Lastly, to quality the performance of land-cover changed pixels, we obtained the proposal of [Stehman et al. \(2021\)](#) in assessing the LCMAP annual land-cover products 1985-2017, that is, the validation pixels were grouped into “changed” and “unchanged” categories and the corresponding confusion matrix were calculated. Meanwhile, to minimize the imbalance in the sample size of “change” and “no-change” samples, the metrics of F1 score was supplemented as:

$$F1 = \frac{P.A. \times U.A.}{P.A. + U.A.} \times 2 \times 100\% \quad (5)$$

### Section 4.3 Accuracy assessment based on two third-party regional validation datasets

Table 4 further analyzed the confusion matrix of land-cover changed and unchanged pixels in GLC\_FCS30D using LCMAP\_Val dataset. It should be noted that the land-cover changed samples in the LCMAP\_Val was still sparse, that is, the size of changed samples cannot support the land-cover change analysis over specific land-cover changes. Similarly, Stehman et al. (2021) also grouped the land-cover types into ‘No change’ and ‘change’ types for analyzing the land-cover changes. In this study, using the ‘changed’ and ‘unchanged’ validation points in LCMAP\_Val, the O.A. of the GLC\_FCS30D reached the 90.49±0.45%. In particular, the unchanged land-cover pixels played a dominant role and reached the high P.A. of 92.84% and U.A. of 96.28%. In contrast, the P.A. and U.A. of concerned land-cover changed pixels were 72.26±2.04% and 56.62±2.00%, and its F1 score was 63.49%.

**Table 4.** The confusion matrix of changed and unchanged pixels in GLC\_FCS30D dataset using LCMAP\_Val datasets.

	Unchanged	Changed	Total	P.A. (SE)	F1
Unchanged	82.21	6.34	88.55	92.84(0.42)	94.53
Changed	3.18	8.27	11.45	<b>72.26(2.04)</b>	63.49
Total	85.39	14.61			
U.A. (SE)	96.28(0.32)	<b>56.62(2.00)</b>			
O.A. (SE)			90.49(0.45)		

Table 7 presented the confusion matrix of changed and unchanged pixels using the LUCAS validation datasets. The overall accuracy of the GLC\_FCS30D reached 90.36±0.38%, the P.A. and U.A. of the changed pixels were 52.86±2.04% and 73.31±2.00%, and the corresponding F1 score was 61.43%. In contrast, the unchanged land-cover pixels reached the high P.A. and U.A., and both two metrics exceeded 90%. Thus, the changed land-cover pixels were more difficult to capture comparing with these unchanged areas. Similarly, [Stehman et al. \(2021\)](#) also found that the accuracy metrics of changed pixels were greatly lower than that of unchanged pixel.

**Table 7.** The confusion matrix of changed and unchanged pixels in GLC\_FCS30D using time-series LUCAS datasets across the Europe Union.

	Unchanged	Changed	Total	P.A. (SE)	F1
Unchanged	82.69	2.79	85.48	96.73	94.49
Changed	6.84	7.68	14.52	52.86	61.43
Total	89.53	10.47			
U.A. (SE)	92.36(0.36)	73.31(1.74)			
O.A. (SE)		90.36(0.38)			

Stehman, S. V., Pengra, B. W., Horton, J. A., and Wellington, D. F.: Validation of the U.S. Geological Survey's Land Change Monitoring, Assessment and Projection (LCMAP) Collection 1.0 annual land cover products 1985–2017, *Remote Sensing of Environment*, 265, 112646, <https://doi.org/10.1016/j.rse.2021.112646>, 2021.

Meanwhile, we also highlighted the necessity of strengthening the accuracy analysis for land-cover changed pixels in our future works in Section 4.5 as:

The time-series accuracy variability is only analyzed in two regions, so its performance in more complex areas (such as Africa and Asia) needs to be further investigated. Thus, future work would be paid on collecting long-term time-series validation data sets for more regions, and on building a long time-series global validation dataset, and then analyzed the accuracy metrics of the land-cover changed pixels for all land-cover types.

As well as global product comparison (e.g., ESACCI and MODIS) should be given and discussed.

Based on your suggestion, the comparisons with ESACCI and MCD12Q1 have been added in two typical areas in Section 4.4 as:

#### 4.4 The comparisons with other global land-cover dynamic products

Figure 12 gave the qualitative comparisons between our GLC\_FCS30D and two widely used land-cover dynamic datasets (CCI\_LC and MCD12Q1) during 2001-2020 in the Indo-China Peninsula, in which experienced evident land-cover changes in forest deforestation and urban expansion. In terms of the urban expansion, three datasets revealed the quick urbanization in the mega-city of Bangkok, and the CCI\_LC underestimated the impervious surface areas in 2001 comparing with two other datasets. Meanwhile, the GLC\_FCS30D also captured more spatial details (such as: rural building and road networks) than CCI\_LC and MCD12Q1 because of its high spatial resolution of 30 m.

As the most significant deforestation, the CCI\_LC showed the worst performance because 1) it underestimated the forest covers in the 2001 (the rectangle region 1), that is, some forests were wrongly labeled as the croplands; 2) some deforested forests cannot be captured during the period of 2001-2020 in rectangle region 2 (R2), and their deforested forest area was less than that of GLC\_FCS30D and MCD12Q1; and 3) there was obvious misclassification problem between forest and wetland in 2000 (the rectangle region 3, R3). Then, the MCD12Q1 also suffered the omission error for forest in rectangle region 1, namely, the captured forest area in 2000 was lower than their actual areas in natural-color imagery. As for the evident deforestation in the region 2, we can find that almost all forest pixels changed to the other land-cover types (savanna and grassland), which was obviously deviated from the actual situation, thus, MCD12Q1 over-estimated the forest deforestation. Meanwhile, the time-series MCD12Q1 showed various land-cover distributions in the R3, which indicated that the MCD12Q1 performed lower mapping accuracy and temporal stability for these wetland areas. In comparison,

the GLC\_FCS30D achieved the best performance in capturing the spatial distribution of forest in 2000, forest deforestation during 2001-2020, and wetland stability.

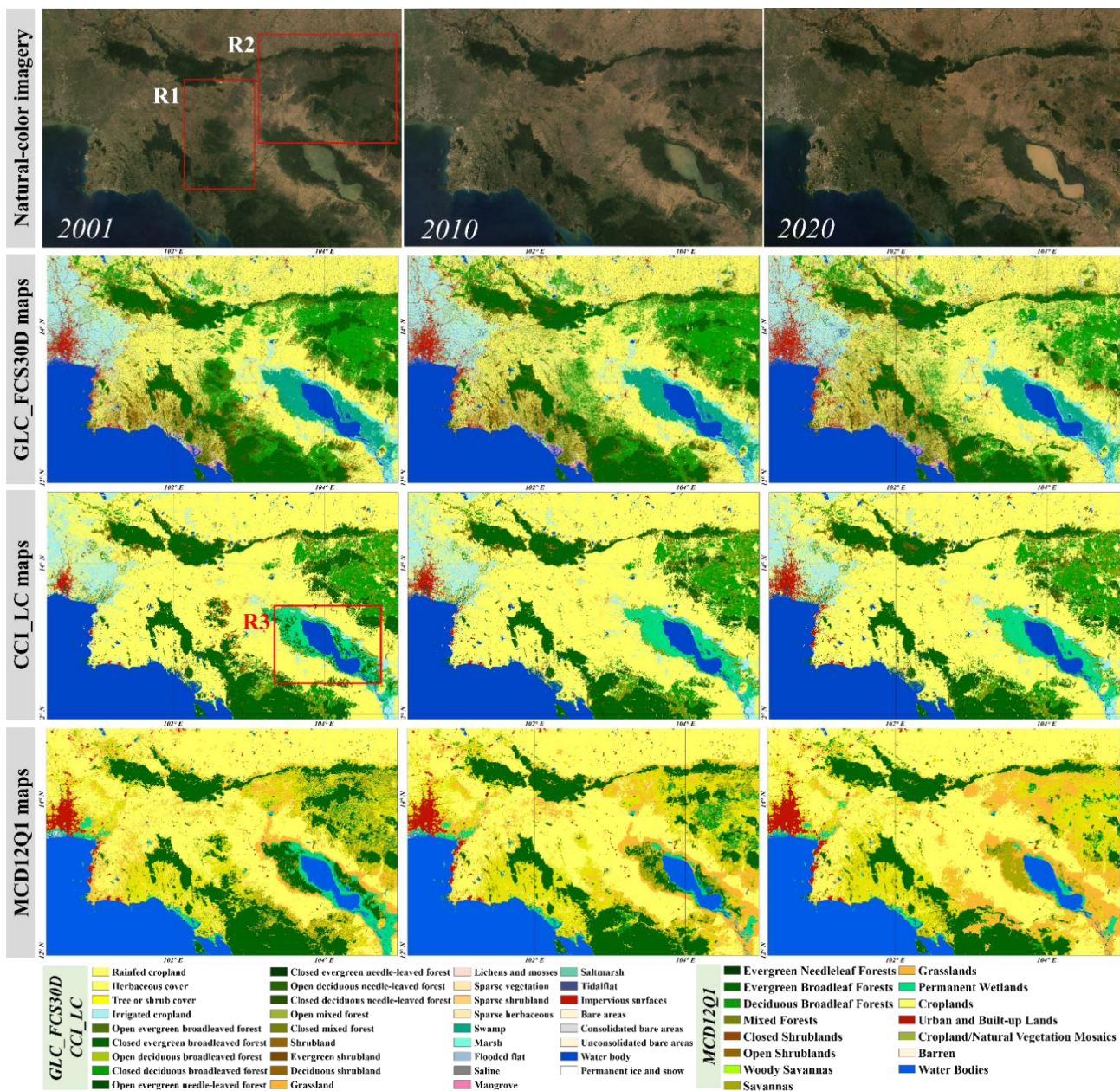


Figure 12. The comparisons between GLC\_FCS30D with CCI\_LC and MCD12Q1 land-cover dynamic products in Indo-China Peninsula during 2001-2020. The natural-color imagery are composited from the time-series Landsat imagery.

Figure 13 showed another comparison example about three datasets in Paraguay, South America, and the most evident land-cover change was the deforestation and cropland incensement according to the time-series natural-color Landsat imagery. In terms of the spatial distribution, the consistency between GLC\_FCS30D and CCI\_LC was higher, while the MCD12Q1 was obviously different from the other two datasets. A large amount of deciduous broadleaved forests were labeled as the savanna and woody savanna, and most croplands were identified as the grasslands in the MCD12Q1, which mainly because of the difference of classification system. Then, as for the land-cover change areas, the GLC\_FCS30D performed the highest accuracy and captured the

richer spatial details. For example, the deforestation intensity during 2010-2020 was significantly greater than that during 2001-2010, and the GLC\_FCS30D also revealed the regular deforestation caused by human factors. In contrast, the CCI\_LC and MCD12Q1 failed to capture the deforestation during 2010 and 2020, and the small and fragmented changes (caused by human activities) also cannot be captured.

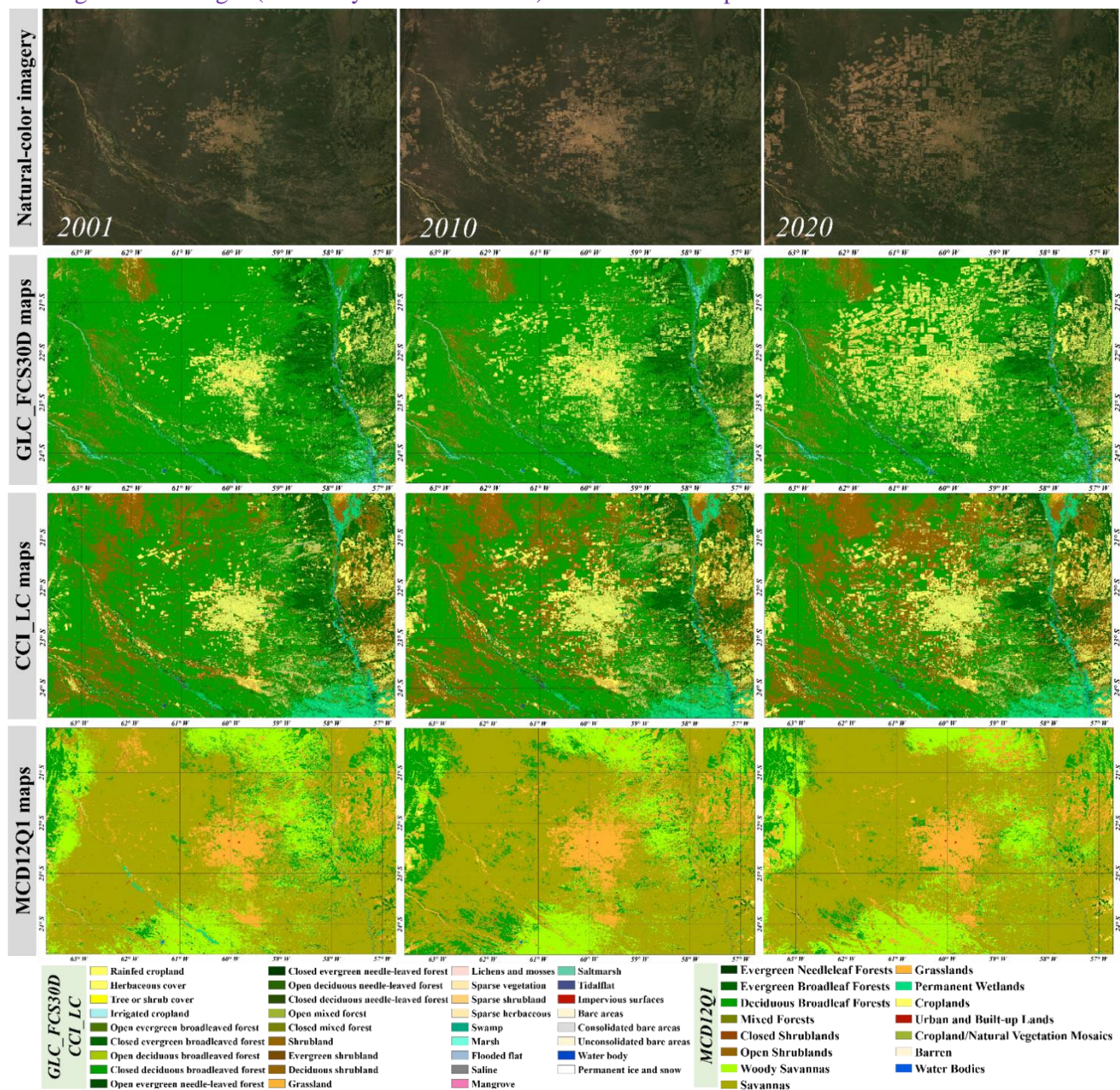


Figure 13. The comparisons between GLC\_FCS30D with two time-series land-cover dynamic datasets in Paraguay, South America, during 2001-2020.

## Response to comments

**Paper #:** essd-2023-320

**Title:** GLC\_FCS30D: The first global 30-m land-cover dynamic monitoring product with a fine classification system from 1985 to 2022 using dense time-series Landsat imagery and continuous change-detection method

**Journal:** Earth System Science Data

## Reviewer #2

The authors present a very detailed manuscript on the generation of a global 30-m land cover product. It is original in the spatio-temporal density of Landsat satellite imagery used to generate annual maps over nearly 30 years. I recommend this paper for publication. There is one major issue that needs to be addressed and a number of minor or editorial issues to address:

Great thanks for the positive comments. The manuscript has been further improved based on your and another reviewers' comments and suggestions.

### Major change:

Both the Continuous Change Detection and Classification (CCDC) Algorithm and the Random Forest Algorithm for subsequent land cover classification use several hyperparameters. Both models will be sensitive to the hyperparameters selected. As a minimum, the hyperparameters selected for both models need to be clearly defined and justified (this is already partially done for the CCDC algorithm). However, to fully justify the use of hyperparameters, sensitivity analysis should be provided of the values used, and validation that the optimum or a favorable set of hyperparameters values have been selected.

Great thanks for the comment. Based on your suggestion and another reviewer's comment, the analysis of how to determine the parameters of CCDC algorithm have been added in the Section 3.2 as:

Next, the CCD was also a multi-parameter change detection model and demonstrated to be sensitive to the parameter settings (Xiao et al., 2023; Zhu and Woodcock, 2014b). The CCDC algorithm on the Google Earth Engine platform (ee.Algorithms.TemporalSegmentation.Ccdc) contained three key adjustable parameters: minObservations, chiSquareProbability and minNumOfYearScaler. Zhu et al. (2019) analyzed the relationships between the omission error and commission error of land-cover changes with the variability of three parameters in the United States, and found their values affected the change detection accuracy. In this study, we also investigated the sensitivity between parameter settings with the change detection accuracies in Figure S1 (seen the Supplement material) using the time-series points from LCMAP\_Val and LUCAS datasets after partly sampling. Notably, the sensitivity analysis was implemented in two large-areas for ensure the feasibility of optimal parameters, that is, which will be suitable for other areas in land-cover change detection. The results also showed the CCD is a parameter-sensitive algorithm and the optimal parameter values were 5, 0.95 and 2-year for minObservations, chiSquareProbability and minNumOfYearScaler.



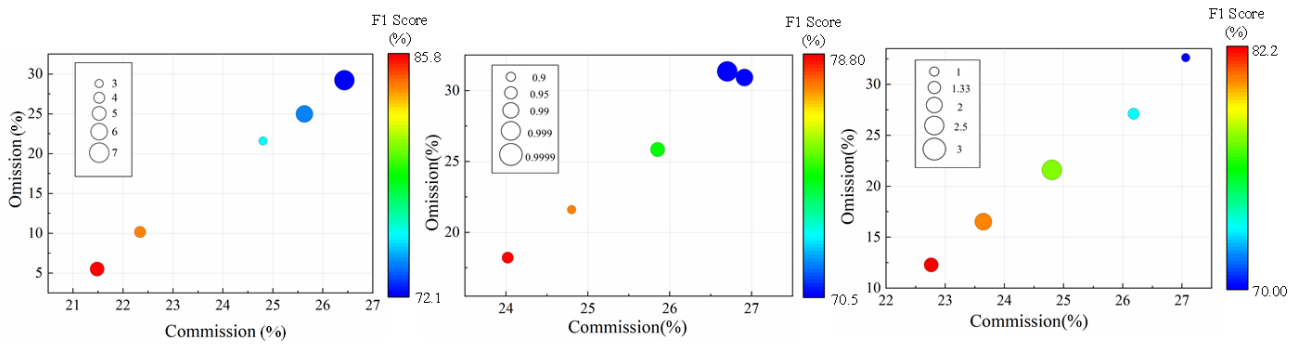


Figure S1. The sensitive analysis between the omission error and commission error with the minObservations, chiSquareProbability and minNumOfYearScaler using the time-series points from LCMAP\_Val and LUCAS datasets after partly sampling.

Xiao, Y., Wang, Q., Tong, X., and Atkinson, P. M.: Thirty-meter map of young forest age in China, *Earth Syst. Sci. Data*, 15, 3365-3386, <https://doi.org/10.5194/essd-15-3365-2023>, 2023.

Zhu, Z., Zhang, J., Yang, Z., Aljaddani, A. H., Cohen, W. B., Qiu, S., and Zhou, C.: Continuous monitoring of land disturbance based on Landsat time series, *Remote Sensing of Environment*, <https://doi.org/10.1016/j.rse.2019.03.009>, 2019.

As for the parameters of random forest classifier, it only contains two adjustable parameters (the number of decision tree (Ntree) and predicted variables (Mtry)), and many previous studies have quantitatively or theoretically analyzed the influence of the parameters on the classification accuracy, and found that the classification accuracy was less sensitive to the selection of Ntree and Mtry. Thus, the default recommended setting of 500 and the square of the total number of input features were used. Correspondingly, the descriptions of how to determine these two parameters have been added in the manuscript as:

Thus, the RF algorithm was used to combine the training samples and multisourced features for updating the changed pixels. The RF algorithm allows for adjusting two key parameters (**the number of decision tree (Ntree) and predicted variables (Mtry)**), and previous studies have quantitatively investigated the relationships between classification accuracy with the settings of these two parameters. Both theoretical and experimental results indicated that the selection of Mtry and Ntree had little influence on the classification accuracy (Belgiu and Drăguț, 2016; Du et al., 2015). Thus, the default recommended values of 500 for Ntree and the square of the total number of input features for Mtry were used based on previous studies (Belgiu and Drăguț, 2016; Zhang et al., 2019).

#### Minor or editorial changes:

3. Introduction/ methods – various mentions of model ‘accuracy’ is used. This includes, but is not limited to lines 31-32, 69 and 155. Please be specific on the accuracy metric(s) used.

Great thanks for the comment. The ‘overall accuracy’ in the whole manuscript (line 31-32, 69 and 155) is an accuracy metric in the confusion matrix. In this manuscript, three accuracy metrics including: overall accuracy (O.A.), producer’s accuracy (P.A.) and user’s accuracy (U.A.) have been used and the corresponding formulas are also added in the Section 3.4 (accuracy assessment) as:

The validation process for the GLC\_FCS30D dataset follows the recommended guidelines proposed by [Pontus Olofsson \(2014\)](#). These guidelines encompass two key components: area estimation (nonsite-specific

accuracy) and accuracy assessment (site-specific accuracy). The site-specific accuracy assessment mainly focuses on estimating the confusion matrix and calculating some accuracy metrics including overall accuracy (O.A.), producer's accuracy (P.A.), user's accuracy (U.A.) and the corresponding standard errors using a poststratified estimator ([Pontus Olofsson, 2014](#)).

$$P.A._k = \frac{p_{kk}}{\sum p_k}, U.A._k = \frac{p_{kk}}{\sum p_k}, O.A. = \sum_{k=1}^m p_{kk} \quad (4)$$

Where  $p_{kk}$  was the proportion of the area mapped as class  $k$  that had reference class  $k$ ,  $\sum p_k$  and  $\sum p_k$  were the proportion of the area mapped as class  $k$  and the proportion of the reference area as class  $k$ , and the  $m$  denoted the number of land-cover types. Afterwards, because there is currently no global long-time series validation dataset, we used 84526 global validation points to assess the accuracy metrics of the GLC\_FCS30D dataset in 2020 and used two third-party datasets to analyze the time-series accuracy variations. The GLC\_FCS30D adopts a fine classification system containing 35 subcategories, for which we applied an analysis protocol into two validation systems (the level-0 classification system containing 10 major land-cover types and the LCCS level-1 validation system containing 17 land-cover types) to comprehensively understand the GLC\_FCS30D dataset quality. The relationship between Level-0 and LCCS level-1 validation systems is explained in Table 1. Lastly, to quality the performance of land-cover changed pixels, we followed the proposal of [Stehman et al. \(2021\)](#) in assessing the LCMAP annual land-cover products 1985-2017, that is, the validation pixels were grouped into “changed” and “unchanged” categories and the corresponding confusion matrix were calculated. Meanwhile, to minimize the imbalance in the sample size of “change” and “no-change” samples, the metrics of F1 score was supplemented as:

$$F1 = \frac{P.A. \times U.A.}{P.A. + U.A.} \times 2 \times 100\% \quad (5)$$

4. Line 24- The use of the phrase ‘In specific’ is awkward and I suggest changing e.g. ‘Specifically’ or ‘In particular...’

Great thanks for the suggestion. The ‘In specific’ has been changed as ‘Specifically’ and ‘In particular’ through the whole manuscript.

5. Line 201- ‘The first time series validation set was assessed the performance...’ remove ‘was’.

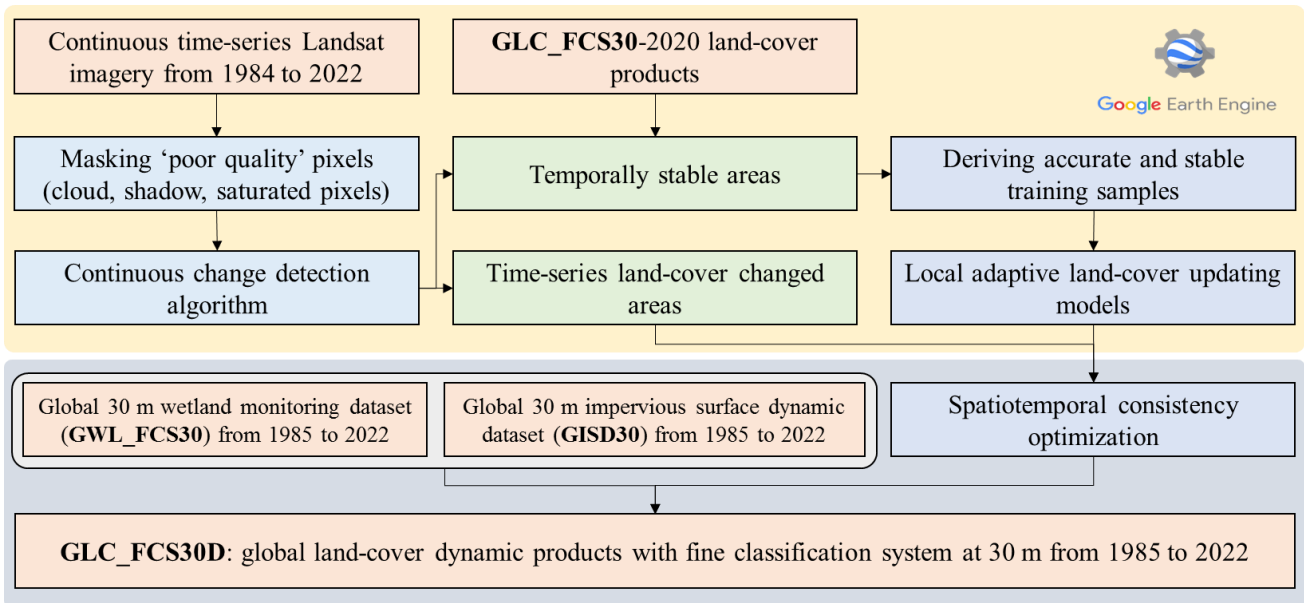
Great thanks for pointing out the mistake. It has been corrected.

6. Line 205- Change ‘It developed by combining...’ to ‘It was developed by combining...’

Great thanks for pointing out the mistake. It has been corrected.

7. Figure 2: This Figure is very useful for help the reader understand the main processes carried out in this project. Please add the shortened names of each dataset to the flow chart to make it even easier for the reader to follow the text.

Great thanks for the comment. Based on your suggestion, the shortened names of each dataset have been added and also bolded into the flowchart as:



8. Figure 2: You refer to masking ‘poor quality’ pixels. Please be more specific on this.

Great thanks for the comment. The ‘poor quality’ refers to these cloud, shadow and saturated pixels, as well as the Scan Line Corrector Off pixels in Landsat 7, which was added in the revision version.

Does this just include applying a cloud mask, or does it also consider issues with the Scan Line Corrector on Landsat 7, for example. What cloud mask was used.

Yes, the Scan Line Corrector Off pixels are also masked. Specifically, the ‘poor-quality’ pixels were masked using the CFmask algorithm, which was demonstrated to achieve high accuracy and great robustness for masking these ‘poor-quality’ pixels.

How did you account for pixels that may be under light cloud/ haze which may not be picked up by a cloud mask (e.g. does the CCDC intend to overcome this?)

In terms of these light cloud/haze pixels, actually, the Tmask algorithm, which was integrated into the CCDC algorithm in the GEE platform, was used to further minimize their effects.

**The explanations have been added in Section 3 as:**

Before detecting the land-cover changed pixels, all ‘poor quality’ pixels (cloud, shadow and saturated pixels, as well as the Scan Line Corrector Off pixels in Landsat 7) in the continuous time-series Landsat imagery were firstly masked using the CFmask algorithm, which was demonstrated to achieve the overall accuracy of 96.4% and was adopted by the USGS as official cloud- and shadow detection algorithm (Zhu et al., 2015; Zhu and Woodcock, 2012). Then, in terms of these residual cloud pixels (light cloud and haze contaminated pixels), the Tmask (multiTemporal mask) algorithm, which used the temporal information from these clear-sky pixels to improve the cloud-detection capability (Zhu and Woodcock, 2014a), was used to mask the residual cloud pixels. It should be noted that the Tmask has been integrated into the CCD algorithm on the GEE platform as ee.Algorithms.TemporalSegmentation.Ccdc(), that is, the effect of ‘poor-quality’ pixels were minimized.

9. Table 1: Please add the abbreviations for each land cover type to this table (at later points you refer to Table 1 as containing these).

Great thanks for the suggestion. The abbreviations of each land-cover type have been into the Table 1 as:

Basic system	classification	Level-1 validation system		Fine classification system	Id		
Cropland	CRP	Rainfed cropland	RCP	Rainfed cropland	10		
				Herbaceous cover cropland	11		
				Tree or shrub cover cropland	12		
		Irrigated cropland	ICP	Irrigated cropland	20		
Forest	FST	Evergreen broadleaved forest	EBF	Closed evergreen broadleaved forest	51		
				Open evergreen broadleaved forest	52		
				Deciduous broadleaved forest	BDF	Closed deciduous broadleaved forest	61
						Open deciduous broadleaved forest	62
		Evergreen needleleaved forest	ENF	Closed evergreen needleleaved forest	71		
				Open evergreen needleleaved forest	72		
				Deciduous needleleaved forest	DNF	Closed deciduous needleleaved forest	81
						Open deciduous needleleaved forest	82
		Mixed-leaf forest	MFT	Closed mixed-leaf forest	91		
				Open mixed-leaf forest	92		
		Shrubland	SHR	Shrubland	SHR	Shrubland	120
						Evergreen shrubland	121
Deciduous shrubland	122						
Grassland	GRS	Grassland	GRS	Grassland	130		
Tundra	TUD	Lichens and mosses	LMS	Lichens and mosses	140		
Wetland	WET	Inland wetland	IWL	Swamp	181		
				Marsh	182		
				Flooded flat	183		
				Saline	184		
		Coastal wetland	CWL	Mangrove	185		
				Salt marsh	186		
				Tidal flat	187		
Impervious surface	IMP	Impervious surface	IMP	Impervious surface	190		
Bare areas	BAL	Sparse vegetation	SVG	Sparse vegetation	150		

				Sparse shrubland	152
				Sparse herbaceous cover	153
		Bare areas	BAL	Bare areas	200
				Consolidated bare areas	201
				Unconsolidated bare areas	202
Water body	WTR	Water body	WTR	Water body	210
Permanent snow and ice	PSI	Permanent snow and ice	PSI	Permanent snow and ice	220

10. Line 357- please provide more information on the indicator function, or at least a reference.

Great thanks for the comment. The description of the indicator function has been strength and the reference is also added as:

“and the  $I()$  denotes the indicator function for the equation of the status between two pixels. Namely, if  $L_{x',y',t'}$  was equal to the  $L_{x,y,t}$ , then the value of indicator function was 1, otherwise it was equal to 0 (Kenny, 2003)”

Kenny, Q. Y.: Indicator function and its application in two-level factorial designs, *The Annals of Statistics*, 31, 984-994, <https://doi.org/10.1214/aos/1056562470>, 2003.

11. Figure 7- the very thick lines corresponding to pixels with a stable land cover overwhelm this image and make it difficult for the reader to decipher the most dominant types of land cover change. Please either rescale the image or consider removing the lines corresponding to no land cover change to make it easier for the reader to assess the dominant types of land cover change.

Great thanks for the comment. To make the Sankey diagram clear, the layout has been changed. The updated Figure 7 are following:

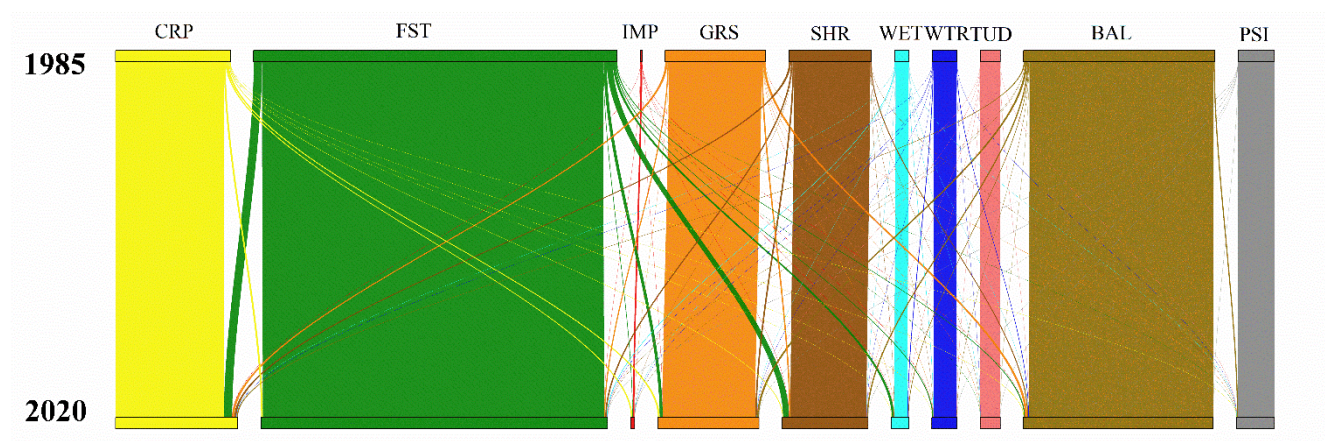


**Figure 7.** Sankey diagrams of the global land-cover changes during 1985-2022 in the GLC\_FCS30D dataset.

12. Table 2 and 3- please use a method to highlight the relative performance of your algorithms. For example use a colour ramp or make particular values bold.

Great thanks for the comment. Since the ESSD journal does not allow colormaps to be added to the Table, some particular accuracy values (mentioned in the manuscript) have been bolded in Table 2 and 3 based on your suggestion as:

**Table 2.** Error matrix of the GLC\_FCS30D dataset in 2020 based on the level-0 basic classification system. The reported Producer's Accuracy (P.A.) and User's Accuracy (U.A.) come with their corresponding standard errors (SE) shown in parentheses.

Reference	Map										O.A. = 80.88% ( $\pm 0.27\%$ )	
	CRP	FST	GRS	SHR	WET	WTR	TUD	IMP	BAL	PSI	Total	P.A.(SE)
CRP	15.442	0.792	0.679	0.388	0.086	0.027	0	0.174	0.117	0	17.704	87.22(0.54)
FST	0.513	28.712	0.315	0.811	0.371	0.021	0.008	0.063	0.113	0.002	30.93	<b>92.83(0.31)</b>
GRS	1.035	1.166	5.906	1.181	0.231	0.011	0.084	0.051	1.181	0.01	10.855	<b>54.41(1.02)</b>
SHR	0.555	1.798	0.863	5.392	0.161	0.013	0.019	0.05	0.502	0.002	9.356	<b>57.63(1.09)</b>
WET	0.068	0.465	0.156	0.157	4.047	0.347	0.031	0.021	0.222	0.001	5.516	73.37(1.27)
WTR	0.04	0.086	0.019	0.017	0.302	3.305	0.008	0.012	0.039	0.002	3.831	86.28(1.12)
TUD	0.01	0.123	0.168	0.167	0.018	0.03	2.444	0.002	0.473	0.02	3.454	70.76(1.65)
IMP	0.084	0.058	0.024	0.04	0.001	0.006	0.002	5.043	0.024	0	5.283	95.45(0.61)
BAL	0.13	0.049	0.783	0.585	0.043	0.045	0.577	0.048	9.239	0.131	11.628	79.45(0.8)
PSI	0	0.004	0.03	0.005	0	0.023	0.001	0	0.03	1.351	1.443	93.63(1.38)
Total	17.877	33.251	8.943	8.743	5.259	3.828	3.176	5.464	11.94	1.52		
U.A.(SE)	86.38 (0.55)	86.35 (0.4)	66.05 (1.07)	61.68 (1.11)	76.96 (1.2)	86.33 (1.35)	76.97 (1.6)	92.29 (0.77)	77.38 (0.82)	88.89 (1.72)		

**Table 3.** Error matrix of the GLC\_FCS30D dataset in 2020 based on the LCCS level-1 validation system. The reported Producer's Accuracy (P.A.) and User's Accuracy (U.A.) come with their corresponding standard errors (SE) shown in parentheses.

Reference	RCP	ICP	EBF	DBF	ENF	DNF	MFT	SHR	GRS	LMS	SVG	IWL	CWL	IMP	BAL	WTR	PSI	Total	P.A. (SE)
RCP	12.225	<b>1.023</b>	0.239	0.358	0.102	0.016	0.009	0.382	0.66	0	0.078	0.056	0.005	0.124	0.028	0.001	0	15.332	79.7(0.7)
ICP	0.397	1.932	0.026	0.016	0.005	0	0	0.01	0.025	0	0.012	0.029	0.005	0.052	0	0.018	0	2.527	76.45(1.81)
EBF	0.2	0.048	9.091	1.098	0.262	0.103	<b>0.151</b>	0.371	0.084	0	0.012	0.136	0.028	0.029	0.001	0.004	0	11.514	78.96(0.82)
DBF	0.187	0.016	0.632	6.838	0.537	0.294	<b>0.396</b>	0.235	0.144	0.002	0.019	0.077	0.002	0.025	0.005	0.004	0.002	9.054	75.53(0.97)
ENF	0.046	0.004	0.174	0.316	5.681	0.328	<b>0.439</b>	0.128	0.034	0.006	0.043	0.094	0	0.008	0.01	0.01	0	6.895	<b>82.39(0.98)</b>
DNF	0.008	0	0.002	0.13	0.245	1.854	<b>0.073</b>	0.071	0.053	0	0.011	0.025	0	0.001	0.007	0.002	0	2.414	76.79(1.85)
MFT	0.004	0	<b>0.019</b>	<b>0.176</b>	<b>0.234</b>	<b>0.013</b>	<b>0.828</b>	0.014	0.004	0	0	0.010	0.05	0	0.001	0	0	1.308	<b>58.29(1.53)</b>
SHR	0.518	0.042	0.299	0.9	0.328	0.131	0.034	5.44	0.871	0.019	0.441	0.157	0.005	0.05	0.065	0.013	0.002	9.438	57.63(1.09)
GRS	0.947	0.097	0.167	0.582	0.209	0.154	0.024	1.191	5.958	0.085	0.974	0.229	0.006	0.052	0.217	0.008	0.01	10.95	54.41(1.02)
LMS	0.006	0.004	0.001	0.022	0.044	0.053	0.001	0.168	0.169	2.465	0.379	0.02	0.001	0.002	0.098	0.026	0.02	3.484	70.76(1.65)
SVG	0.064	0.01	0.008	0.006	0.007	0.01	0.001	0.397	0.462	0.025	2.71	0.012	0	0.013	0.643	0.002	0.024	4.399	61.6(1.57)
IWL	0.01	0.002	0.044	0.029	0.103	0.022	0.002	0.048	0.017	0.008	0.042	2.673	0.024	0.001	0.012	0.224	0	3.263	<b>81.91(1.45)</b>
CWL	0.004	0.002	0.008	0.002	0.004	0.002	0.004	0.008	0.006	0	0.008	0.188	1.476	0.007	0.007	0.059	0	1.783	<b>82.77(1.92)</b>
IMP	0.074	0.011	0.008	0.008	0.037	0.002	0	0.041	0.024	0.002	0.014	0.004	0	5.087	0.01	0.004	0	5.329	95.45(0.61)
BAL	0.048	0.01	0.002	0.004	0.002	0.001	0	0.193	0.328	0.557	0.582	0.043	0.002	0.035	5.384	0.029	0.108	7.33	73.45(1.11)
WTR	0.014	0.024	0.014	0.014	0.019	0.008	0.006	0.011	0.016	0.007	0.011	0.168	0.114	0.011	0.019	3.054	0.002	3.509	87.04(1.22)
PSI	0	0	0	0.001	0.002	0	0	0.005	0.03	0.001	0.011	0	0	0	0.019	0.023	1.363	1.455	93.65(1.37)
Total	14.757	3.224	10.753	10.56	7.833	3.724	1.97	8.711	8.883	3.179	5.353	3.927	1.668	5.497	6.526	3.482	1.532		
U.A. (SE)	82.85 (0.67)	<b>59.92</b> (1.85)	84.55 (1.75)	64.76 (1)	72.52 (1.08)	49.77 (1.76)	<b>39.34</b> (1.38)	62.44 (1.11)	67.07 (1.07)	77.55 (1.59)	<b>50.63</b> (1.47)	<b>68.07</b> (1.6)	<b>88.49</b> (1.68)	92.54 (0.76)	82.5 (1.01)	87.73 (1.19)	88.96 (1.72)		
O.A.	73.04% ( $\pm 0.30\%$ )																		

13. Results and discussion are very thorough although there is no mention to coastal regions which will be areas of major change detectable at 30 m resolution.

Great thanks for the comment. Yes, we completely agree that the coastal regions experienced obvious land-cover changes. To intuitively understand these coastal changes, an example in Yellow River Estuary Delta was also added in the Figure 8 and the corresponding descriptions as:

Lastly, the Yellow River Delta, as one of the typical coastal regions, was selected to understand the GLC\_FCS30D for capturing these coastal land-cover changes. Obviously, the land-cover changes in the GLC\_FCS30D can be concluded into three aspects: 1) a large amount of flooded flats and flat flats were reclaimed as the aquaculture ponds, especially after 2000; 2) the mouth of the Yellow River turned from south to north (black rectangle), that is, there were large land-cover changes between tidal/flooded flats, water bodies and salt marshes; 3) a lot of impervious surfaces encroached the coastal water-bodies and flats. In short, if we combine real time-series remote-sensing observation data, the GLC\_FCS30D effectively captures the spatiotemporal changes of the land surface.

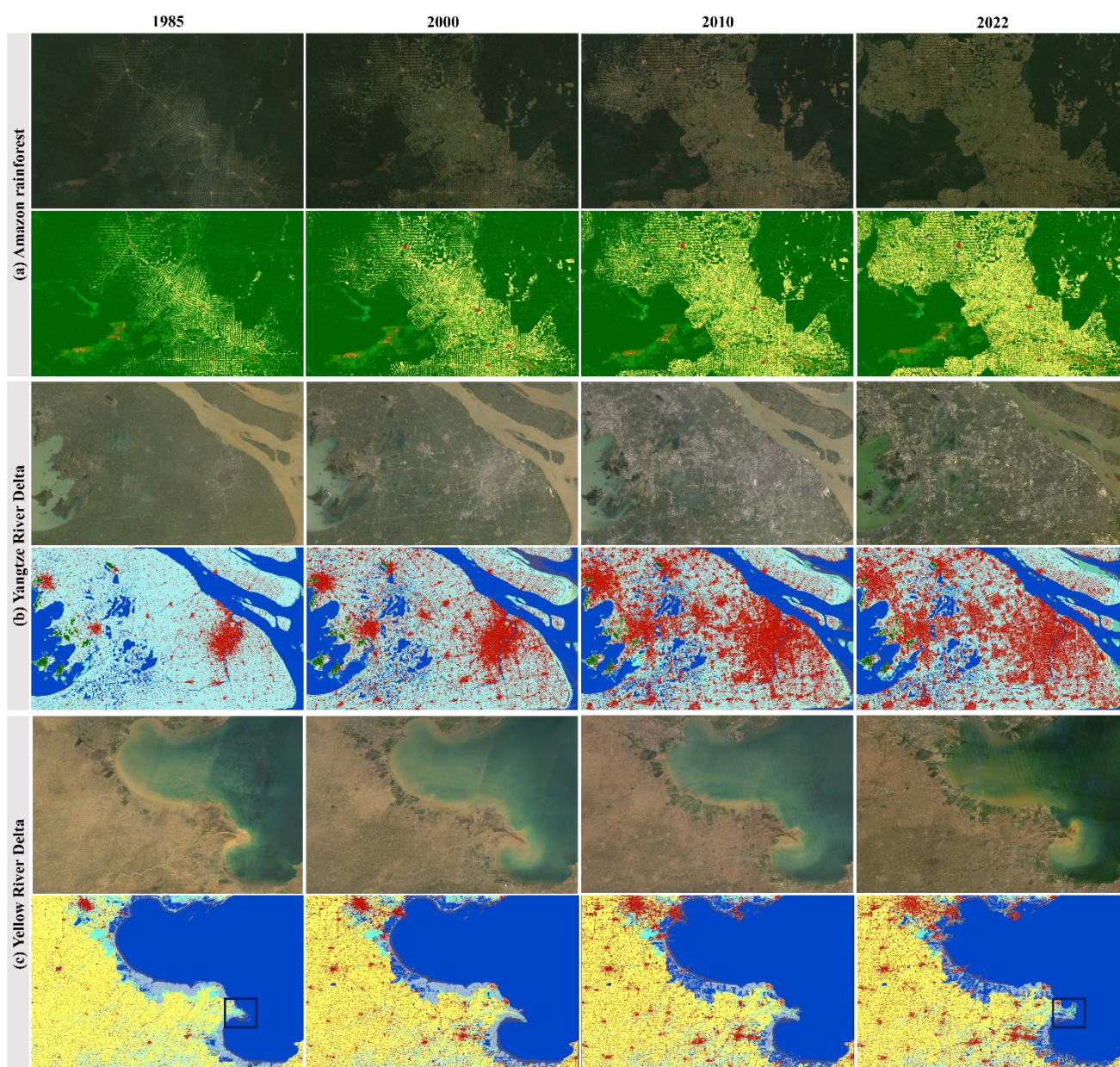


**Figure 8.** Three typical enlargements of land-cover changes in the GLC\_FCS30D from 1985 to 2022 in (a) the Amazon rainforest, (b) the Yangtze River Delta in China, and (c) the Yellow River Delta in China. The color-

coded legend is like the global map in Figure 4. In each case, the natural-color imagery from 1985 to 2022 is a composite taken from Landsat imagery.

14. Overall, I enjoyed reading this paper. The analysis was very thorough and easy to follow.

Great thanks for the positive comments. The analysis has been further improved based on your and another reviewer's comments.



# GLC\_FCS30D: The first global 30-m land-cover dynamic monitoring product with a fine classification system from 1985 to 2022 using dense time-series Landsat imagery and continuous change-detection method

Xiao Zhang<sup>1,2</sup>, Tingting Zhang<sup>1,4</sup>, Hong Xu<sup>5</sup>, Wendi Liu<sup>1,2,3</sup>, Jinqing Wang<sup>1,2,3</sup>, Xidong Chen<sup>6</sup> and Liangyun Liu<sup>1,2,3,\*</sup>

1 International Research Center of Big Data for Sustainable Development Goals, Beijing 100094, China

2 Key Laboratory of Digital Earth Science, Aerospace Information Research Institute, Chinese Academy of Sciences, Beijing 100094, China

3 School of Electronic, Electrical and Communication Engineering, University of Chinese Academy of Sciences, Beijing 100049, China

4 College of Geomatics, Xi'an University of Science and Technology, Xi'an 710054, China

5 The High-Tech Research & Development Center (HTRDC) of the Ministry of Science & Technology, Beijing 100044, China

6 Future Urbanity & Sustainable Environment (FUSE) Lab, The University of Hong Kong, Hong Kong, 999007, China

\* Corresponding author Email: liuly@radi.ac.cn

## Abstract

Land cover change has been identified as an important cause or driving force of global climate change and is a significant research topic. Over the past few decades, global land-cover mapping has progressed, however, long time-series global land-cover change monitoring data are still sparse, especially at 30-m resolution. In this study, GLC\_FCS30D is described as the first global 30-m land-cover dynamic monitoring dataset, containing 35 land-cover subcategories and covering the period of 1985–2022 with 26 time-steps (maps updated every five years before 2000 and annually after 2000). GLC\_FCS30D has been developed using continuous change detection and all available Landsat imagery based on the Google Earth Engine platform. ~~In specific~~Specifically, we first take advantage of the continuous change-detection model and full time-series Landsat observations to capture the time-points of changed pixels and identify the temporally stable areas. Then, we apply a spatiotemporal refinement method to derive the globally distributed and high-confidence training samples from these temporally stable areas. Next, locally adaptive classification models are used to update the land-cover information for the changed pixels, and a temporal-consistency optimization algorithm is adopted to improve their temporal stability and suppress some false changes. Further, the GLC\_FCS30D product is validated using 84,526 globally distributed validation samples in 2020 and achieves an overall accuracy of 80.88% ( $\pm 0.27\%$ ) for the basic classification system (10 major land-cover types) and 73.2404% ( $\pm 0.30\%$ ) for the LCCS level-1 validation system (17 LCCS land-cover types). Meanwhile, two third-party time-series validation datasets in the United States and Europe Union are also collected for analyzing accuracy variations, and the results show that the GLC\_FCS30D offers significant stability for time-series accuracy variation and achieves the mean accuracies of 79.50% ( $\pm 0.50\%$ ) and 81.91% ( $\pm 0.09\%$ ) over the two regions. Last, we conclude the global land-cover change information from GLC\_FCS30D dataset, namely, the forest and cropland variations dominate global land cover change over past 37 years, and net loss of forests reaches about 2.5 million km<sup>2</sup> and net gain in cropland area is approximately 1.3 million km<sup>2</sup>. Therefore, the novel GLC\_FCS30D is an accurate time-series land-cover dynamic monitoring product benefiting from its diverse classification system, high spatial resolution

and the long time span of 1985–2022, thus, it will effectively support global climate change research and promote sustainable development analysis. The GLC\_FCS30D datasets are available via <https://doi.org/10.5281/zenodo.8239305> (Liu et al., 2023).

**Keywords:** GLC\_FCS30D, 1985-2022, Land-cover change, Landsat, change detection, Google Earth Engine

## 45 1. Introduction

Land cover data are important and necessary for supporting sustainable development goals, maintaining biodiversity, and monitoring natural resources (Liu et al., 2021b; Potapov et al., 2022). The land cover changes directly or indirectly influence the global climate patterns and the speed and magnitude of climate change (Song et al., 2018) and increasingly affects biogeochemical cycles, the carbon cycle, and Earth's energy balance (Foley et al., 2005; Hong et al., 2021; Winkler et al., 2021). Since the industrial revolution, under the dual pressure of global climate change and human activities, global land cover has undergone drastic changes. According to a Global Carbon Project report in 2020, since the industrialization period, land cover and land use changes have contributed to approximately 25% of global greenhouse gas emissions (Friedlingstein et al., 2020), and this trend is exacerbated with the ongoing increase in population and per capita energy consumption (Xian et al., 2022). Therefore, understanding and studying land cover changes are of vital significance for addressing global environmental changes, promoting sustainable development, and safeguarding the Earth's ecological environment.

Remote-sensing techniques, with periodic Earth observation capability and archived massive long-term observation data since 1972, provide the most cost-effective and practical solutions for long time-series large-area land-cover change monitoring. In the past few decades, with the continuous improvement of remote sensing technology and storage and computing capabilities, global land-cover change monitoring (GLCCM) has transitioned from 1-km spatial resolution to fine resolution of 30-m or 10-m and from single-phase mapping to long-term monitoring (Ban et al., 2015; Friedl et al., 2010; Friedl et al., 2022; Giri et al., 2013). In the early stage, GLCCM mainly relied on the time-series MODIS, AVHRR, and Project for Onboard Autonomy (PROBA)-V imagery; for example, Sulla-Menashe et al. (2019) generated a global 500-m annual land-cover products (MCD12Q1) from 2001 to present using time-series MODIS imagery with an overall accuracy of 73.6%. Defourny et al. (2018) integrated time-series PROBA-V and Medium Resolution Imaging Spectrometer (MERIS) observations to develop a global 300-m annual land-cover dynamic dataset (CCI\_LC) from 1992 to 2020 with an overall accuracy of 71.5%. These coarse land-cover change products comprehensively captured the spatial patterns of various land-cover types and quantified the global land-cover changes caused by human and natural activities. However, they still had major limitations especially in regions with intense human activity and high spatial heterogeneity because these broken and heterogeneous land-cover changes cannot be captured by coarse-resolution satellite observations (Hansen et al., 2013; Herold et al., 2008; Liu et al., 2021b; Zhang et al., 2021c).

Recently, benefitting from the free access to fine-resolution satellite imagery and powerful computing and storage capabilities, especially after the rise of cloud computing [such as Google Earth Engine (Gorelick et al., 2017) and Microsoft Planetary Computer], fine-resolution land-cover dynamic monitoring is experiencing rapid development. Correspondingly, numerous national and global 30-m land-cover dynamic products have been developed (Homer et al., 2020; Liu et al., 2021a; Potapov et al., 2022; Yang and Huang, 2021; Zhang et al., 2022). For example, Yang and Huang (2021) used China's land-use/cover datasets (CLUDs) as the prior dataset

and then combined multitemporal classification and spatiotemporal consistency post-processing method to develop an annual 30-m land cover dataset (CLCD) for China from 1990 to 2019. Similarly, [Liu et al. \(2021a\)](#) combined pixel-based classification and spatiotemporal post-processing method to generate the first global 30-m land-cover change products. However, many studies have demonstrated that multiperiod independent  
85 classifications lead to significant classification error accumulation in time-series land-cover change monitoring ([Sulla-Menashe et al., 2019](#); [Zhu, 2017](#)). For example, [Xian et al. \(2022\)](#) stated that the independent classification strategy suffered the constraints of post-processing requirements, for ensuring the temporal consistency of land-cover change maps. Therefore, although GLCCM has progressed significantly over the past few decades, an accurate global 30-m land-cover change-detection product generated by an efficient land-cover  
90 change method is still urgently required.

One of the greatest challenges for large-area land-cover change detection is to select the optimal algorithm to capture the land-cover changes from time-series observations ([Healey et al., 2018](#); [Zhu, 2017](#)). Over past few decades, a series of change-detection algorithms have been proposed for monitoring forest disturbance ([Huang et al., 2009](#); [Jin et al., 2023](#); [Kennedy et al., 2007](#); [Kennedy et al., 2010](#); [Qin et al., 2021](#)), urban expansion ([Liu et al., 2019](#); [Zhang et al., 2021a](#)), cropland dynamics ([Dong et al., 2015](#); [Potapov et al., 2021](#)), and land-cover  
95 changes ([Bullock et al., 2019](#); [Jin et al., 2017](#); [Verbesselt et al., 2010](#); [Zhu et al., 2019](#)). However, most of them were only suitable for regional land-cover change monitoring and some of the algorithms needed prior knowledge (such as for urban expansion). [Zhu \(2017\)](#) systematically reviewed the performances and limitations of various change-detection methods based on multitemporal satellite data, and further explained that the high  
100 temporal frequency and multivariate change-detection algorithms are more suitable for large-area and long time-series land-cover changes after solving a problem with a huge amount of computation. Similarly, [Xian et al. \(2022\)](#) and [Liu et al. \(2019\)](#) concluded that dense and continuous change-detection methods had higher accuracy and more robustness than traditional change-detection methods for capturing multiple, complicated changes.

Continuous Change Detection and Classification (CCDC) algorithm, a classical change-detection method  
105 based on dense time-series observations proposed by ([Zhu and Woodcock, 2014b](#)), is widely used for regional and national land-cover monitoring ([Xian et al., 2022](#); [Xie et al., 2022](#)). It used all available Landsat observations to build time-series regression models and then captured the outliers by analyzing the differences between the actual observations and model estimations. [Zhu and Woodcock \(2014b\)](#) demonstrated that the CCDC algorithm attained a general accuracy of 90% and temporal accuracy of 80% for capturing land-cover changes. Thus, it  
110 has been adopted by the United States Geological Survey (USGS) as the official algorithm for monitoring land-cover changes over the United States ([Pengra et al., 2016](#)). For example, [Xian et al. \(2022\)](#) implemented the CCDC algorithm and all available Landsat data to develop annual land-cover change products over the contiguous United States (CONUS) for 1985–2017 with an overall accuracy of 82.5%.

In summary, over the past decades, land-cover mapping and monitoring has made significant progress;  
115 however, time-series global 30-m land-cover dynamic products derived from change-detection algorithms are still lacking. In this study, we had the following three aims: 1) use the continuous change-detection algorithm and full time-series Landsat observations to generate the first global 30-m land-cover dynamic products with fine classification system (GLC\_FCS30D) from 1985 to 2022, which contains 35 fine land-cover subcategories with 26 time-steps (maps updating every five years before 2000 and annually after 2000); 2) quantify the land-  
120 cover changes and analyze the spatiotemporal change patterns of various land-cover types based on the

developed GLC\_FCS30D dataset; and 3) quantitatively analyze the performance of the GLC\_FCS30D product using multisourced validation datasets.

## 2. Datasets

### 2.1 Continuous Landsat imagery from 1984 to 2022

125 All available Landsat imagery from 1984 to 2022, covering Landsat 5 Thematic Mapper (TM), Landsat 7  
Enhanced Thematic Mapper Plus (ETM+), Landsat 8 Operational Land Imager (OLI), and Landsat 9 OLI  
missions, was collected via the GEE cloud-computing platform. Specific measures were taken to build a high-  
quality continuous time-series Landsat collection. First, all Landsat images underwent atmospheric correction  
to convert them to surface reflectance using the Landsat Ecosystem Disturbance Adaptive Processing System  
130 (LEDAPS) and Land Surface Reflectance Code (LaSRC) methods ([Vermote, 2007](#); [Vermote and Kotchenova,  
2008](#)). Then, ~~the CFmask algorithm, which and has high accuracy and good robustness in cloud and shadow  
detection and is also the official cloud and shadow detection algorithm of the USGS, was applied to mask poor-  
quality observations, including cloud, shadow, and saturated pixels.. Last,~~ although the Landsat 5, 7, 8, and 9  
missions share similar spectral bands, the wavelength differences between the ETM+ and OLI cannot be ignored.  
135 Relative radiometric normalization was applied to the TM and ETM+ imagery using the transformation  
coefficients suggest by [Roy et al. \(2016\)](#).

### 2.2 Global land-cover dataset at 30 m for the year of 2020

140 The global 30-m land-cover product with fine classification system in 2020 (GLC\_FCS30-2020), is the  
baseline for generating training samples and identifying land-cover information in the temporally stable regions  
in Section 3. The GLC\_FCS30 dataset was developed using locally adaptive classifications and confident and  
globally distributed training samples in their developed global spatiotemporal spectra library, and then validated  
to reach an overall accuracy of 82.5% with the basic validation system ([Zhang et al., 2021b](#)). Cross-comparisons  
with other land-cover products showed obvious advantages for the GLC\_FCS30 in mapping accuracy and  
diversity of land-cover types. The GLC\_FCS30-2020 dataset is freely available at  
145 <https://doi.org/10.5281/zenodo.4280923> ([Liu et al., 2020](#)).

### 2.3 Global impervious surface dynamic dataset at 30 m from 1985 to 2022

150 Many studies found that high spatiotemporal heterogeneity and broken constructs of impervious surface  
caused high uncertainty and difficulty in monitoring their dynamics ([Gong et al., 2019](#); [Zhang et al., 2022](#)), and  
change detection methods also face issues of both missed detections and false alarms when applied to the  
dynamic monitoring of heterogeneous impervious surfaces. Thus, we independently produced a time-series  
global impervious surface dynamic dataset at 30 m (GISD30) during 1985–2022 and then overlaid this thematic  
dataset on the GLC\_FCS30D dataset to ensure their high confidence in the impervious surface dynamics. The  
GISD30 dataset was developed by combining the sample migration, spectra generalization and local adaptive  
modeling methods, and then optimized by the spatiotemporal-consistency correction method ([Zhang et al.,  
155 2022](#)). It was validated to attain the mean overall accuracy of 90.1% over the globe and to perform better than  
other similar products in capturing the changes in impervious surfaces over time and across different types of  
landscapes. At the same time, third-party validation also indicated that GISD30 exhibited superior performance  
among similar global 30-meter impervious surface products ([Wang et al., 2022](#)).

### 2.4 Global 30-m wetland datasets from 1985 to 2022

160 Like the impervious surface, the global wetland dynamic dataset is independently produced because the  
reflectance spectra of the wetland and phenological variations changed daily with the water levels. The  
continuous change-detection method would suffer serious commission and omission errors for wetland dynamic  
monitoring (Gallant, 2015). In this study, the GWL\_FCS30 (global 30-m wetland map with a fine classification  
system) wetland dataset from 1985 to 2022, developed by integrating the automatic sample extraction method,  
165 a stratified classification strategy, and time-series Landsat observations (Zhang et al., 2023), would be  
superimposed on the GLC\_FCS30D land-cover dynamic dataset. The GWL\_FCS30 was quantitatively assessed  
to the mean overall accuracy of 86.44% using 25708 validation points, and demonstrated the highest level of  
performance among other wetland products when it came to capturing the spatial patterns of wetlands during  
cross-comparisons (Zhang et al., 2023). GWL\_FCS30 further splits the wetland into seven wetland  
170 subcategories (four inland and three coastal subcategories), and would be overlaid directly onto the  
GLC\_FCS30D dataset not only improves the monitoring accuracy of wetland but also enriches the number of land  
cover types (in Table 1).

## 2.5 Validation datasets

To comprehensively analyze the accuracy metrics for the GLC\_FCS30D dataset, two types of validation  
175 datasets were collected, including: an independent global validation dataset from 2020 and two third-party time-  
series validation datasets for the United States and the European Union.

### 2.5.1 Global validation dataset

A total of 84,526 globally distributed validation samples are collected to analyze the accuracy metrics for  
the GLC\_FCS30D dataset in 2020, and their spatial distributions are illustrated in Figure 1. Intuitively, the  
180 spatial patterns of the global validation dataset are consistent with the actual global land-cover situation.  
Specifically, to ensure the confidence and rationality of the validation datasets, several measures are taken,  
which were explained in detail in our previous work (Zhao et al. (2023)). First, a stratified random sampling  
method is applied by combining the landscape heterogeneity, population density data and Köppen climate  
groups, which effectively increases the sample size in the heterogeneous landscapes and for these rare land-  
185 cover types. Second, for each validation sample, the land-cover type is determined through independent  
interpretation by trained interpreters after combining high-resolution aerial photography, multitemporal Landsat  
images, and other relevant ancillary datasets (such as: vegetation coverage, tree height, phenological curves, ,  
and terrain characteristics). Independent interpretation software has also been developed based on the GEE  
platform (<https://eliza-ting.users.earthengine.app/view/crd-vit>) for efficiently recognizing the land cover types  
190 of each sample. Third, a quality-controlled operation, based on duplicate interpretations, is further used to ensure  
the confidence level of each validation sample. Each sample is independently labeled by three junior interpreters  
and then double-checked by the senior experts, and validation samples with huge disparities would be discarded.  
In addition, because the impervious surface and wetland datasets have been independently produced and  
validated in our previous works (Zhang et al., 2023; Zhang et al., 2022), the corresponding high-quality  
195 validation samples of these two thematic types are also imported to the global validation datasets.

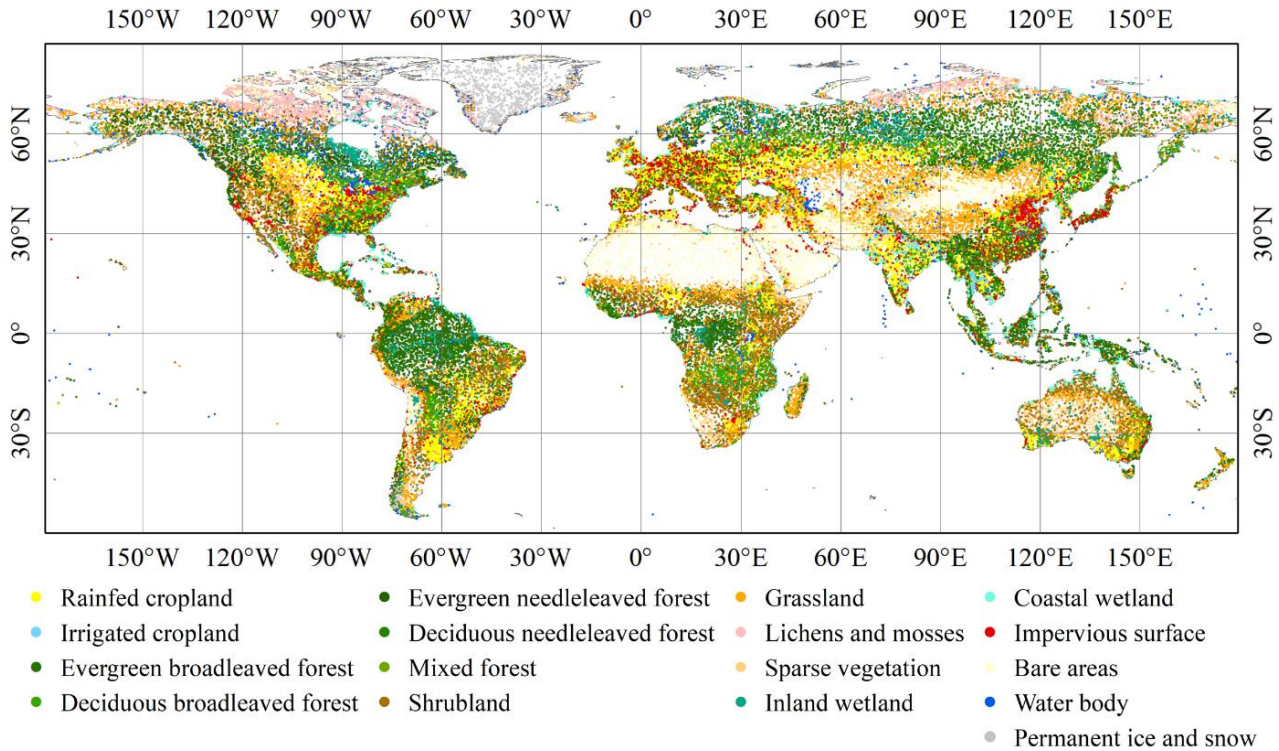


**Figure 1.** Spatial distribution of 84,526 global validation points containing 17 fine land-cover types in the normal year of 2020.

### 2.5.2 Third-party regional time-series validation datasets

200 Due to the great difficulty in the collection of long time-series global validation datasets, we used two third-  
 party regional datasets for the CONUS and the European Union. The first time-series validation dataset ~~was~~  
 assessed the performance of the Land Cover Monitoring, Assessment, and Projection (LCMAP) Collection 1.0  
 annual land cover products (Stehman et al., 2021) (called LCMAP\_Val, [https://www.usgs.gov/special-  
 205 topics/lcmap/validation-data](https://www.usgs.gov/special-topics/lcmap/validation-data)). The LCMAP\_Val consisted of 24,971 validation samples with 30-m spatial  
 resolution and covered time period of 1985 to 2017. It ~~was~~ developed by combining a simple random sampling  
 method and visual interpretation from high-resolution aerial photography, multitemporal Landsat images, as  
 well as other auxiliary datasets. Meanwhile, to guarantee the reliability of each validation sample, the TimeSync  
 auxiliary tool was also adopted to capture the land-cover changes (Stehman et al., 2021). Quality control was  
 implemented through duplicate interpretations (Xian et al., 2022).

210 The second regional validation dataset was the Land Use/Cover Area frame Survey (LUCAS), which is the  
 most comprehensive and largest land-cover validation dataset in the European Union and is freely available at  
<https://land.copernicus.eu/imagery-in-situ/lucas>. It contains 1,090,863 validation points based on a systematic  
 2 km × 2 km grid and covers the period of 2006 to 2018 with an interval of 3 years (d'Andrimont et al., 2020).  
 Five LUCAS surveys in 2006, 2009, 2012, 2015, and 2018 assessed the time-series accuracies of the  
 215 GLC\_FCS30D. The LUCAS is developed from a combination of field observations and photo interpretation  
 (Büttner and Eiselt, 2013; Ballin et al., 2018); thus, it performs with high confidence and also attracts widespread  
 attention in land-cover validations (Gao et al., 2020; Venter et al., 2022).

## 3. Methods

Figure 2 presents a detailed flowchart for monitoring land-cover changes by combining the Continuous Change Detection (CCD) algorithm, proposed by [Zhu and Woodcock \(2014b\)](#), and the local adaptive updating method. Specifically, the flowchart contains four main procedures including: (1) detecting the temporally stable pixels and the time-points of abrupt changes in these changed land-cover pixels from the continuous change-detection model; (2) deriving the spatiotemporally stable training samples by using the spatiotemporal refinement method from GLC\_FCS30 land-cover products and temporally stable masks; (3) building the local adaptive classification models for each local region and then updating the land-cover information in the changed pixels; and (4) using the spatiotemporal consistency optimization method to improve the quality of land-cover change maps and suppress these false changes.

Before detecting the land-cover changed pixels, all ‘poor quality’ pixels (cloud, shadow and saturated pixels, as well as the Scan Line Corrector Off pixels in Landsat 7) in the continuous time-series Landsat imagery were firstly masked using the CFmask algorithm, which was demonstrated to achieve the overall accuracy of 96.4% and was adopted by the USGS as official cloud- and shadow detection algorithm ([Zhu et al., 2015](#); [Zhu and Woodcock, 2012](#)). Then, in terms of these residual cloud pixels (light cloud and haze contaminated pixels), the Tmask (multiTemporal mask) algorithm, which used the temporal information from these clear-sky pixels to improve the cloud-detection capability ([Zhu and Woodcock, 2014a](#)), was used to mask the residual cloud pixels. It should be noted that the Tmask has been integrated into the CCD algorithm on the GEE platform as *ee.Algorithms.TemporalSegmentation.Ccdc()*, that is, the effect of ‘poor-quality’ pixels were minimized.

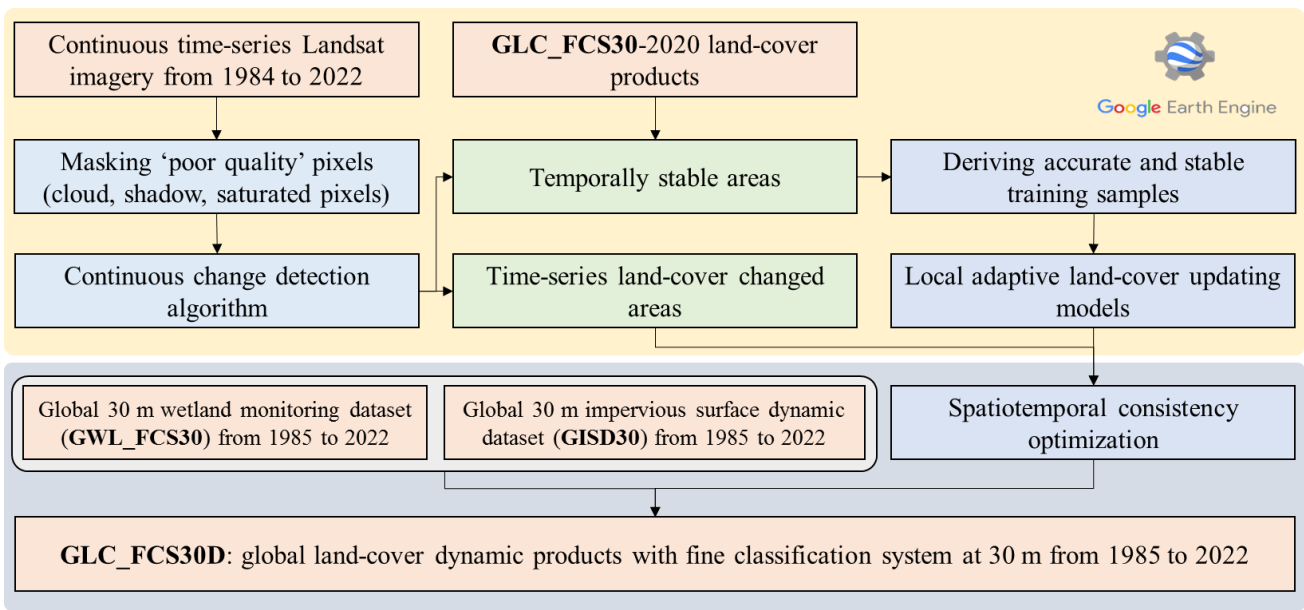


**Figure 2.** The flowchart of the proposed method combining the continuous change-detection (CCD) algorithm and a local adaptive updating algorithm.

### 3.1 The fine classification system used in the GLC\_FCS30D

Determining the classification system is usually a prerequisite for land-cover mapping and monitoring. In this study, as we used the GLC\_FCS30-2020 as the baseline land-cover product, and further overlaid the GWL\_FCS30 dataset on the GLC\_FCS30D to ensure high accuracy in the wetland areas; thus, the fine classification system used in this study would inherit from that of the GLC\_FCS30-2020 and GWL\_FCS30. Table 1 lists the details of the fine classification system. It contains 35 fine land-cover types and has obvious advantages over identifying the forest and wetland subcategories.

**Table 1.** The details of the fine classification system in the GLC\_FCS30D land-cover dynamic dataset.

Basic classification system	Level-1 validation system		Fine classification system	Id	
Cropland	CRP	Rainfed cropland	RCP	Rainfed cropland	10
				Herbaceous cover cropland	11
				Tree or shrub cover cropland	12
		Irrigated cropland	ICP	Irrigated cropland	20
Forest	FST	Evergreen broadleaved forest	EBF	Closed evergreen broadleaved forest	51
				Open evergreen broadleaved forest	52
		Deciduous broadleaved forest	BDF	Closed deciduous broadleaved forest	61
				Open deciduous broadleaved forest	62
		Evergreen needleleaved forest	ENF	Closed evergreen needleleaved forest	71
				Open evergreen needleleaved forest	72
		Deciduous needleleaved forest	DNF	Closed deciduous needleleaved forest	81
				Open deciduous needleleaved forest	82
		Mixed-leaf forest	MFT	Closed mixed-leaf forest	91
				Open mixed-leaf forest	92
Shrubland	SHR	Shrubland	SHR	Shrubland	120
				Evergreen shrubland	121
				Deciduous shrubland	122
Grassland	GRS	Grassland	GRS	Grassland	130
Tundra	TUD	Lichens and mosses	LMS	Lichens and mosses	140
Wetland	WET	Inland wetland	IWL	Swamp	181
				Marsh	182
				Flooded flat	183
				Saline	184
		Coastal wetland	CWL	Mangrove	185
				Salt marsh	186
				Tidal flat	187
Impervious surface	IMP	Impervious surface	IMP	Impervious surface	190
Bare areas	BAL	Sparse vegetation	SVG	Sparse vegetation	150
				Sparse shrubland	152
				Sparse herbaceous cover	153
		Bare areas	BAL	Bare areas	200
				Consolidated bare areas	201
				Unconsolidated bare areas	202
Water body	WTR	Water body	WTR	Water body	210
Permanent snow and ice	PSI	Permanent snow and ice	PSI	Permanent snow and ice	220

### 3.2 Detecting changes using the CCD algorithm and continuous Landsat imagery

In general, land-cover changes can be grouped into three categories including: periodic changes caused by the phenological variability, trend changes driven by natural behavior (such as vegetation growth), and abrupt



255

changes caused by natural or human disturbances (such as deforestation, urban expansion). Thus, capturing these abrupt changes and simultaneously suppressing the periodic and trend changes are the key to land-cover monitoring. In this study, the CCD algorithm (Zhu and Woodcock (2014b)) captured these abrupt changes. The algorithm uses Fourier transformation to fit the time-series observations with the trend term (estimating the trend changes) and harmonic terms (describing the periodic changes) in Eq. (1).

$$\hat{\rho}(i, t) = a_{0,i} + c_{1,i} \times t + \sum_{k=1}^n \left( a_{k,i} \times \cos\left(\frac{2k\pi}{T} t\right) + b_{k,i} \times \sin\left(\frac{2k\pi}{T} t\right) \right) \quad (1)$$

260

where  $\hat{\rho}(i, t)$  represents the predicted value of the  $i$ th band at the  $t$ th Julian day,  $c_{1,i}$  and  $a_{0,i}$  are the regression slope and intercept of the  $i$ th band,  $a_{k,i}$  and  $b_{k,i}$  represent the coefficients of the  $k$ th order harmonic term for the  $i$ th band,  $n$  denotes the number of harmonic terms, and  $T$  is the day number of the year (usually defined as 365). As for how to determine value of  $n$ , Zhu and Woodcock (2014b) explained that higher order harmonic terms have better performance for capturing the periodic variability, but caused overfitting in the time-series model and needed more clear-sky observations to initialize the coefficients of  $a_{k,i}$  and  $b_{k,i}$ . After balancing the advantages and disadvantages of the higher order harmonic terms, we finally chose  $n$  as 3, as suggested by other studies (Xian et al., 2022; Xie et al., 2022).

265

Then, as the CCD is a multivariate change-detection algorithm for capturing the changes of various land-cover types (Zhu (2017)), five Landsat spectral bands (excluding the blue band for minimizing the effects of the atmosphere and clouds), and three spectral indexes [including: NDVI, NDWI, and NBR as given in Eq. (2)] were combined to detect many kind of changes in the Landsat time-series.

$$NDVI = \frac{\rho_{nir} - \rho_r}{\rho_{nir} + \rho_r}, \quad NDWI = \frac{\rho_{green} - \rho_{swir1}}{\rho_{green} + \rho_{swir1}}, \quad NBR = \frac{\rho_{nir} - \rho_{swir1}}{\rho_{nir} + \rho_{swir1}} \quad (2)$$

270

where  $\rho_{green}$ ,  $\rho_r$ ,  $\rho_{nir}$  and  $\rho_{swir1}$  are the green, red, NIR, SWIR1 and SWIR2 spectral bands in the Landsat imagery. Next, to determine the fitted coefficients of the  $k$ th order harmonic term in Eq. (1), the Least Absolute Shrinkage and Selection Operator (LASSO) regression algorithm was applied, which demonstrated better performance than the traditional Ordinary Least Squares method in reducing the overfitting problem and dealing with unevenly distributed and sparse Landsat observations (Zhu and Woodcock (2014b)).

275

280

Next, the CCD was also a multi-parameter change detection model and demonstrated to be sensitive to the parameter settings (Xiao et al., 2023; Zhu and Woodcock, 2014b). The CCDC algorithm on the Google Earth Engine platform (ee.Algorithms.TemporalSegmentation.Ccdc) contained three key adjustable parameters: minObservations, chiSquareProbability and minNumOfYearScaler. Zhu et al. (2019) analyzed the relationships between the omission error and commission error of land-cover changes with the variability of three parameters in the United States, and found their values affected the change detection accuracy. In this study, we also investigated the sensitivity between parameter settings with the change detection accuracies in Figure S1 (seen the Supplement material) using the time-series points from LCMAP\_Val and LUCAS datasets after partly sampling. Notably, the sensitivity analysis was implemented in two large-areas for ensure the feasibility of optimal parameters, that is, which will be suitable for other areas in land-cover change detection. The results also showed the CCD is a parameter-sensitive algorithm and the optimal parameter values were 5, 0.95 and 2-year for minObservations, chiSquareProbability and minNumOfYearScaler.

After modeling the time-series observations using the CCD algorithm, we can analyze the land-cover changes from the differences between actual observations and predicted values in the time-series fitting models. Figure 3 shows three typical scenarios in which land-cover dynamics were modeled by the CCD algorithm. Specifically, Figure 3a illustrates that there was no abrupt break in the whole period and thus only the single time-series model was built, and the pixel was usually labeled as temporally stable. Figure 3b indicates that the pixel underwent an abrupt change and the time-series observations were split into two segments. The time point of the abrupt change occurred around 1996. Figure 3c gives a complicated time-series disturbance example, in which multiple abrupt changes were detected and the time-series observations were split into four segments. The time-series models for segments 1, 2, and 4 showed obvious trend changes.

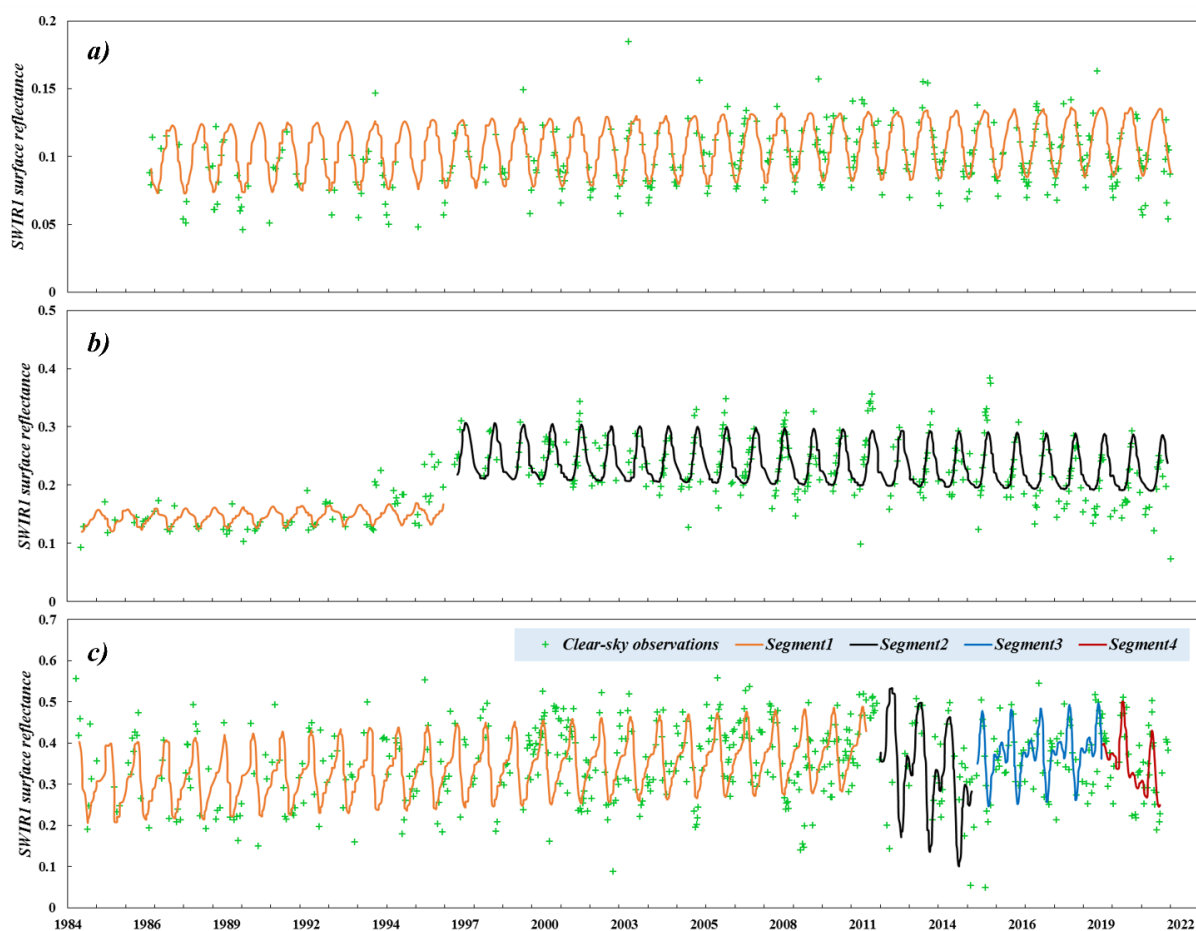


**Figure 3.** Three typical land-cover changes using the continuous change detection (CCD) algorithm and continuous Landsat observations; a) time-series stable land-cover condition; b) one single abrupt change; c) multiple abrupt changes.

### 3.3 Updating changed areas using local adaptive classifications

Using the CCD algorithm and continuous Landsat imagery, we identified the temporally stable pixels and the time points of abrupt changes for the land-cover change pixels. Accurately determining land-cover labels of the changed pixels (or understanding the change process ‘from-to’) is another key procedure for time-series land-cover monitoring. To achieve this goal, we derived spatiotemporally stable training samples (see Section

3.3.1), then updated the changed pixels using multitemporal classifications, and finally minimized the cumulative error caused by independent classifications.

### 305 **3.3.1 Deriving spatiotemporally stable training samples**

Numerous studies demonstrated that the accurateness of the training samples plays a critical role in accurate mapping (Foody and Arora, 2010; Zhang et al., 2020). Visual interpretation can ensure high-confidence samples at the expense of a large quantity of manual participations, so it was not suitable for collecting large-area training samples. An alternative option involved generating training samples by refining existing land-cover products through a series of improvement measures (Zhang et al., 2021b; Zhang et al., 2023). Inspired by the latter option, we combined the GLC\_FCS30-2020 prior dataset and a change-detection mask (derived from the CCD algorithm described in Section 3.2) to obtain the spatiotemporally stable training samples. Specifically, temporally stable areas are known to have higher mapping accuracy (Yang and Huang, 2021; Zhang and Roy, 2017; Zhang et al., 2023); thus, we first used the CCD mask to retain these temporally stable areas in the GLC\_FCS30-2020 maps. Radoux et al. (2014) emphasized that land-cover transition areas usually were subject to more serious misclassification problems and that the homogeneous land-cover pixels had a higher probability of achieving acceptable accuracy. Therefore, we used the morphological erosion filter of 3 pixels  $\times$  3 pixels to refine the GLC\_FCS30-2020 maps into spatially homogeneous areas. After identifying the intersection of temporally stable and spatially homogenous areas, we retained these as the spatiotemporally stable training sample candidates.

Numerous studies have highlighted the importance of training sample balance and distribution, as they significantly influence the mapping performance (Foody, 2009; Jin et al., 2014; Millard and Richardson, 2015). First, in term of the sample distribution, there are two options for training sample distribution including areal-proportional or equal allocation, and former was demonstrate to achieve higher accuracy than the latter option in land-cover mapping especially in complicated land-cover conditions (Jin et al., 2014). However, when using the areal-proportional sampling strategy, the rare land-cover types usually had small sample sizes and would be sacrificed because the aim of land-cover mapping was to achieve a global optimum rather than a local optimum. Thus, the maximum and minimum sample size for abundant and rare land-cover types were suggested as 8000 and 600, came from the study in Zhu et al. (2016), for avoiding the extremes of sample sizes. Next, the GLC\_FCS30-2020 products were split into 961  $5^\circ \times 5^\circ$  geographical tiles, and we used the areal-proportional sampling strategy and sample balancing parameters to allocate the training samples from the spatiotemporally stable areas in each  $5^\circ \times 5^\circ$  geographical tile. Last, the impervious surface and wetland samples were excluded because both have been independently developed as the thematic datasets in Section 2.3 and 2.4.

### **3.3.2 Updating changed areas using local adaptive classifications**

Before building the local adaptive classification models, we must extract useful spectral features from the time-series Landsat observations. In this study, we used multitemporal phenological, texture, and topographical features. Specifically, the multitemporal phenological features were extracted by using the percentile-compositing method, which has fewer constraints than other compositing algorithms (such as the seasonal-based compositing method) while achieving similar mapping accuracy (Azzari and Lobell, 2017). The time-series Landsat spectral bands (five optical bands after excluding atmospherically sensitive blue band) and corresponding spectral indexes [NDVI, NDWI, and NBR in Eq. (2)] were composited into five percentiles (10th, 25th, 50th, 75th, and 90th). Next, in terms of the texture features, our previous study explained that the texture

features had positive contribution on land-cover mapping (Zhang et al. (2021b)), so the gray-level co-occurrence matrix method was used for the 50<sup>th</sup>-percentile-composited NIR band to extract the homogeneity, entropy, 345 dissimilarity, variance, contrast, and correlation. Last, since the land-cover distribution was usually related to the topographical environment, for example, croplands and water bodies are mainly distributed in flat areas, three topographical variables (elevation, slope, and aspect), calculated from a global 30 m DEM dataset (named as: ASTER\_GDEM) (Tachikawa et al., 2011), were also imported. In total, there were 49 multisource features, including 40 phenological spectra features, 6 texture features, and 3 topographical variables.

350 There are two options for global land-cover mapping and updating: global modeling and local adaptive modeling, and our previous studies have explained that local adaptive modeling yields superior results compared to global modeling. This is primarily due to the former's capability to take regional characteristics into account more effectively, leading to increased sensitivity in training samples and higher accuracy in land-cover classification (Zhang et al., 2021b; Zhang et al., 2023; Zhang et al., 2022). Thus, we first inherited the regional 355 gridding style in the GLC\_FCS30 (Zhang et al., 2021b), namely, the global land was divided into 961 5° × 5° geographical tiles. Afterward, the local classification models were independently built for updating the land cover in each tile using the corresponding training samples in the neighboring eight surrounding tiles at 3 × 3 window. The adjacent training samples were imported to increase the continuity of the adjacent land-cover maps.

Last, in the selection of the suitable classification algorithm, random forest (RF) classifier has significant 360 advantages, including: accommodating high-dimensional training features, better ability to deal with the overfitting problem, and higher classification accuracy than other widely used classifiers (Belgiu and Drăguț, 2016; Gislason et al., 2006). Meanwhile, the RF algorithm was also integrated into the internal function library of the GEE cloud platform as *ee.Classifier.smileRandomForest()*. Thus, the RF algorithm was used to combine the training samples and multisourced features for updating the changed pixels. The RF algorithm allows for 365 adjusting two key parameters (the number of decision tree (Ntree) and predicted variables (Mtry)), and previous studies have quantitatively analyzed the relationships between classification accuracy with the value of these two parameters. Both theoretical and experimental results indicated that the selection of Mtry and Ntree had little influence on the classification accuracy (Belgiu and Drăguț, 2016; Du et al., 2015) for which. Thus, the default recommended values of 500 for Ntree and the square of the total number of input features for Mtry were 370 used based on previous studies (Belgiu and Drăguț, 2016; Zhang et al., 2019).

### 3.3.3 Temporal-consistency optimization

To ensure the rationality and consistency of land-cover changes for long time-series, the CCD algorithm was applied to capture the time points of land-cover changes, and then the changed pixels were updated using the local adaptive classifications. In this study, despite our best efforts, it was difficult to completely eliminate 375 classification errors, particularly when dealing with changes over time. To address this issue and enhance accuracy in areas with temporal variations, we employed the temporal consistency optimization method described in Eq. (3). This approach incorporates both temporal and spatial neighboring information to assess homogeneity, thereby reducing potential misclassifications in time-series changed areas.

$$P_{x,y,t} = \frac{1}{N} \left[ \sum_{x'=x-1}^{x+1} \sum_{y'=y-1}^{y+1} \sum_{t'=t-1}^{t+1} I(L_{x',y',t'} = L_{x,y,t}) \right] \quad (3)$$

Where  $P_{x,y,t}$  is the homogeneity probability of the pixel in spatial location  $(x, y)$  and time point  $t$ ; usually, the 380 higher the value of  $P_{x,y,t}$ , the less the classification error effect.  $L_{x,y,t}$  and  $L_{x',y',t'}$  are the land-cover labels of the central pixel and the corresponding spatiotemporal neighboring pixels with a local window of  $3 \times 3 \times 3$ ,

and the  $I()$  denotes the indicator function for the equation of the status between two pixels. Namely, if  $L_{x_i, y_i, t_i}$  was equal to the  $L_{x, y, t}$ , then the value of indicator function was 1, otherwise it was equal to 0 (Kenny, 2003).

In this study, the homogeneity probability was calculated for each changed pixel, and used the threshold of 0.5 (as suggested by and used in the studies of (Li et al., 2015; Zhang et al., 2022) to judge the rationality of land-cover changes. Namely, if the  $P_{x, y, t}$  was less than the threshold, the  $L_{x, y, t}$  would be modified according to the spatiotemporal pixels.

### 3.4 Accuracy assessment

The validation process for the GLC\_FCS30D dataset follows the recommended guidelines proposed by Pontus Olofsson (2014). These guidelines encompass two key components: area estimation (nonsite-specific accuracy) and accuracy assessment (site-specific accuracy). The site-specific accuracy assessment mainly focuses on estimating the confusion matrix and calculating some accuracy metrics including overall accuracy (O.A.), producer's accuracy (P.A.), and user's accuracy (U.A.) and the corresponding standard errors using a poststratified estimator (Pontus Olofsson, 2014).

$$P.A._k = \frac{p_{kk}}{\sum p_{.k}}, U.A._k = \frac{p_{kk}}{\sum p_{k.}}, O.A. = \sum_{k=1}^m p_{kk} \quad (4)$$

Where  $p_{k.}$  was the proportion of the area mapped as class  $k$  that had reference class  $k$ ,  $\sum p_{k.}$  and  $\sum p_{.k}$  were the proportion of the area mapped as class  $k$  and the proportion of the reference area as class  $k$ , and the  $m$  denoted the number of land-cover types. Afterwards, because there is currently no global long-time series validation dataset, we used 84526 global validation points to assess the accuracy metrics of the GLC\_FCS30D dataset in 2020 and used two third-party datasets to analyze the time-series accuracy variations. The GLC\_FCS30D adopts a fine classification system containing 35 subcategories, for which we applied an analysis protocol into two validation systems (the level-0 classification system containing 10 major land-cover types and the LCCS level-1 validation system containing 17 land-cover types) to comprehensively understand the GLC\_FCS30D dataset quality. The ~~correspondence~~ relationship between Level-0 and LCCS level-1 validation systems is explained in Table 1. Lastly, to quality the performance of land-cover changed pixels, we obtained followed the proposal of Stehman et al. (2021) in assessing the LCMAP annual land-cover products 1985-2017, that is, the validation pixels were grouped into "changed" and "unchanged" categories and the corresponding confusion matrix were calculated. Meanwhile, to minimize the imbalance in the sample size of "change" and "no-change" samples, the metrics of F1 score was supplemented as:

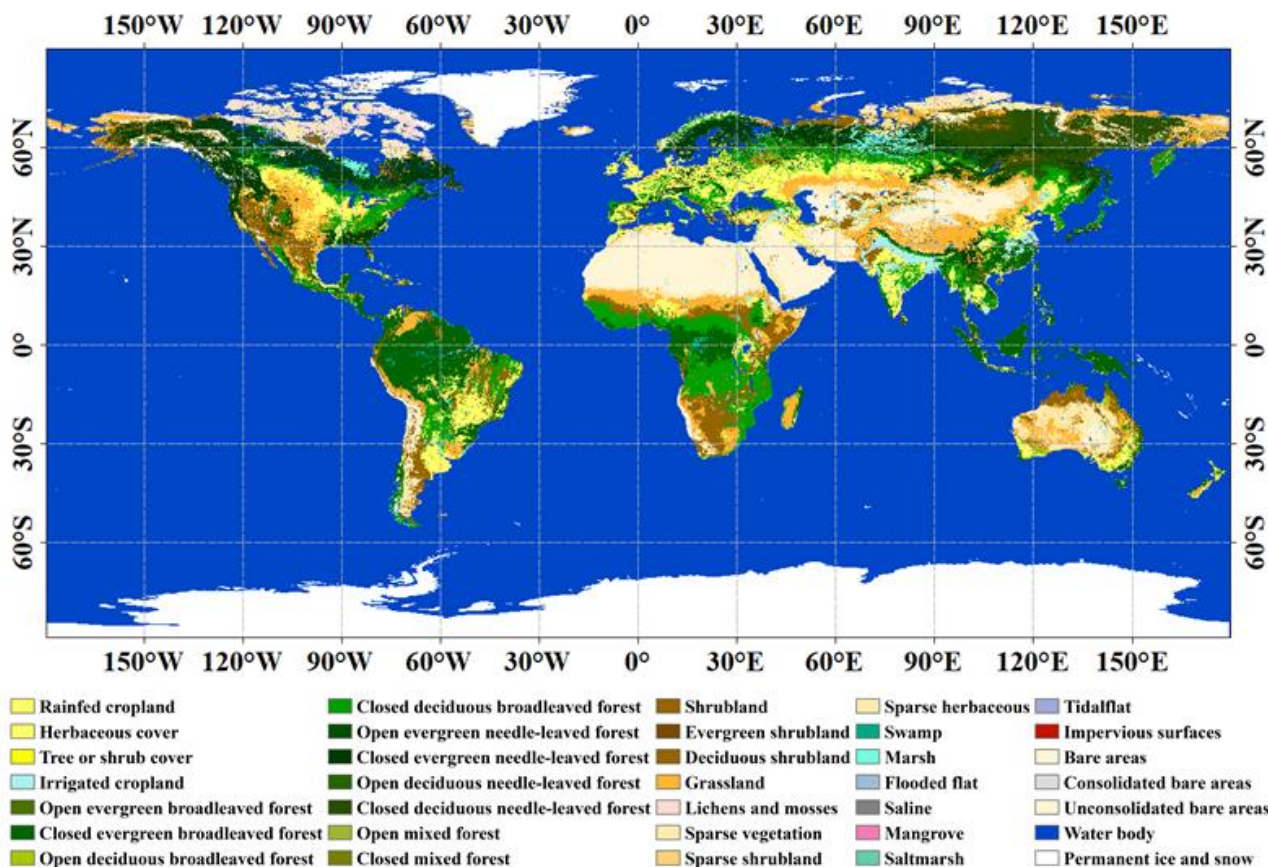
$$F1 = \frac{P.A. \times U.A.}{P.A. + U.A.} \times 2 \times 100\% \quad (5)$$

## 4. Results and discussion

### 4.1 Overview of GLC\_FCS30D maps and their changes

Figure 4 provides an overview of the GLC\_FCS30D dataset in 2022; overall, it aligns with the real-world land-cover patterns on a global scale. Forest, cropland, barren land, and grassland are the dominant land-cover types, and each of them is distributed in the corresponding ecology subregions. For example, needle-leaved forest is mainly concentrated in the high-latitude cold regions while broad-leaved forests are mainly distributed in tropical regions; permanent ice and snow is mainly located in Greenland and high-altitude mountains. The GLC\_FCS30D has significant advantages over other global land-cover datasets in terms of land-cover type

diversity; it contains 35 discrete land-cover types, among which forest and wetland are subdivided into 10 and 7 land-cover subcategories, respectively.



420 **Figure 4.** Overview of the GLC\_FCS30D in 2022 with a color-coded legend derived from the European Space Agency (ESA) Climate Change Initiative land-cover dataset (Defourny et al., 2018).

Figure 5a illustrates the spatial distribution of land-cover change intensity (measuring the proportions of changed pixels in the 0.05° grid) in the GLC\_FCS30D from 1985 to 2022 after upscaling to a resolution of 0.05°. Obviously, global land-cover has experienced significant changes over the past 37 years, mainly in the following three typical areas: 1) tropical rainforest peripheral areas in South America and Southeast Asia, in which deforestation is the dominant cause; 2) wetland and water-body intermingling areas, such as North America and northern Asia, in which water bodies and wetland were transformed into one another due to different annual water levels. In the GLC\_FCS30D the water body land-cover type represents permanent water during the year (it may be wetland in other years). 3) The semi-arid areas in Australia, Central Asia, and western Africa, where land cover (such as sparse vegetation or bare land) is directly affected by precipitation and temperature. For example, if there is sufficient precipitation in the year, the sparse vegetation and some bare land would be covered by grass in semi-arid areas. Similarly, the work of Winkler et al. (2021) revealed that these semi-arid areas experienced serious and frequent land-cover changes. Figure 5b quantitatively counts the changed areas of 10 major land-cover types from 1985 to 2022. Forest and cropland variations dominated global land-cover change. The net loss of forests over the past 37 years reached approximately 2.5 million km<sup>2</sup>, and the decline is steady over time. Conversely, cropland showed a stable increase and the net gain in cropland area is approximately 1.3 million km<sup>2</sup>. Shrubland, wetland, and impervious surface had increased areas of 0.45 million km<sup>2</sup>, 0.40 million km<sup>2</sup>, and 0.37 million km<sup>2</sup>, respectively. The increased shrubland resulted from the

440 recovery of deforested land, and the wetland gains are due to increases in seasonal water bodies. The work of [Pekel et al. \(2016\)](#) emphasized that the global seasonal water bodies, labeled as inland wetland in the GLC\_FCS30D, showed an overall increase.

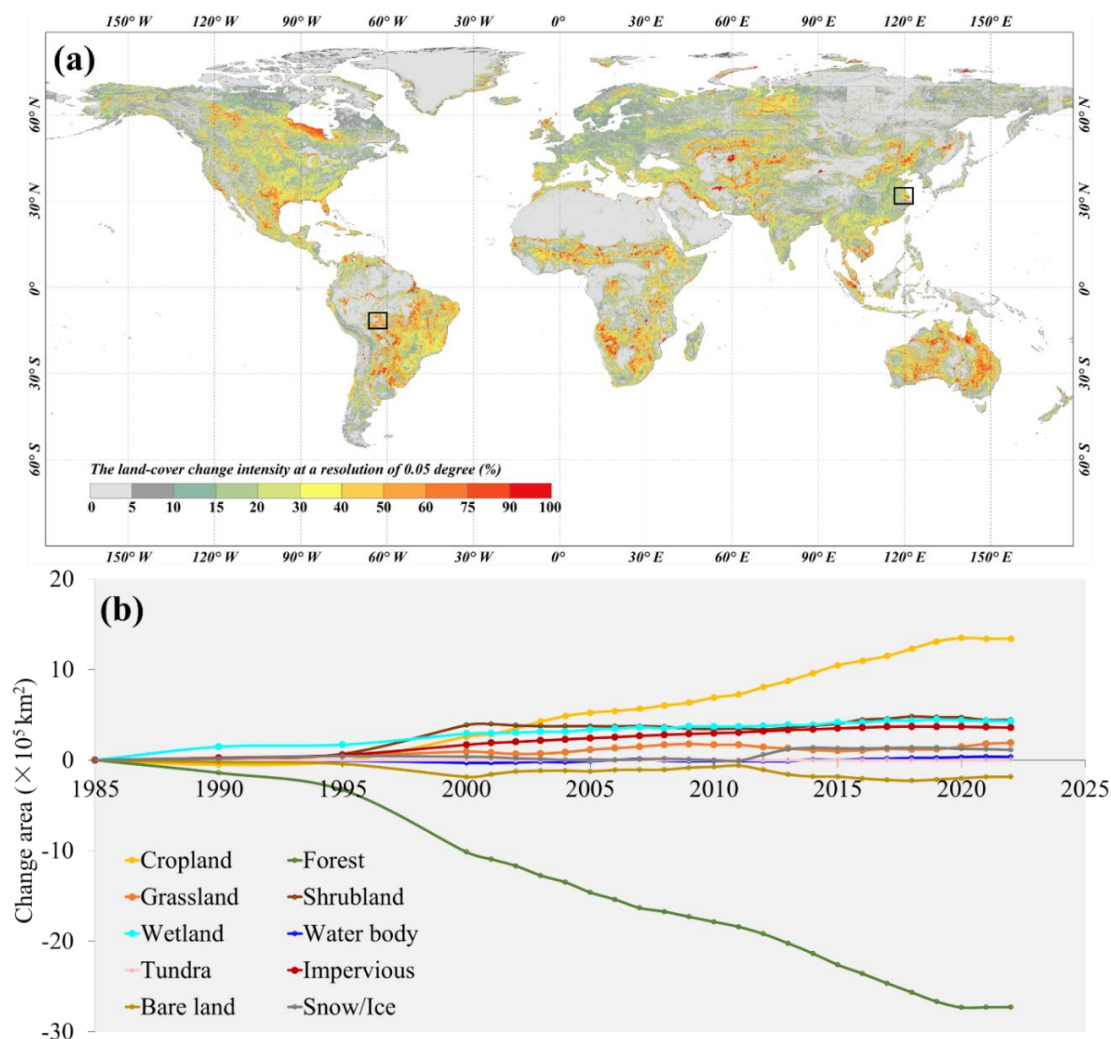
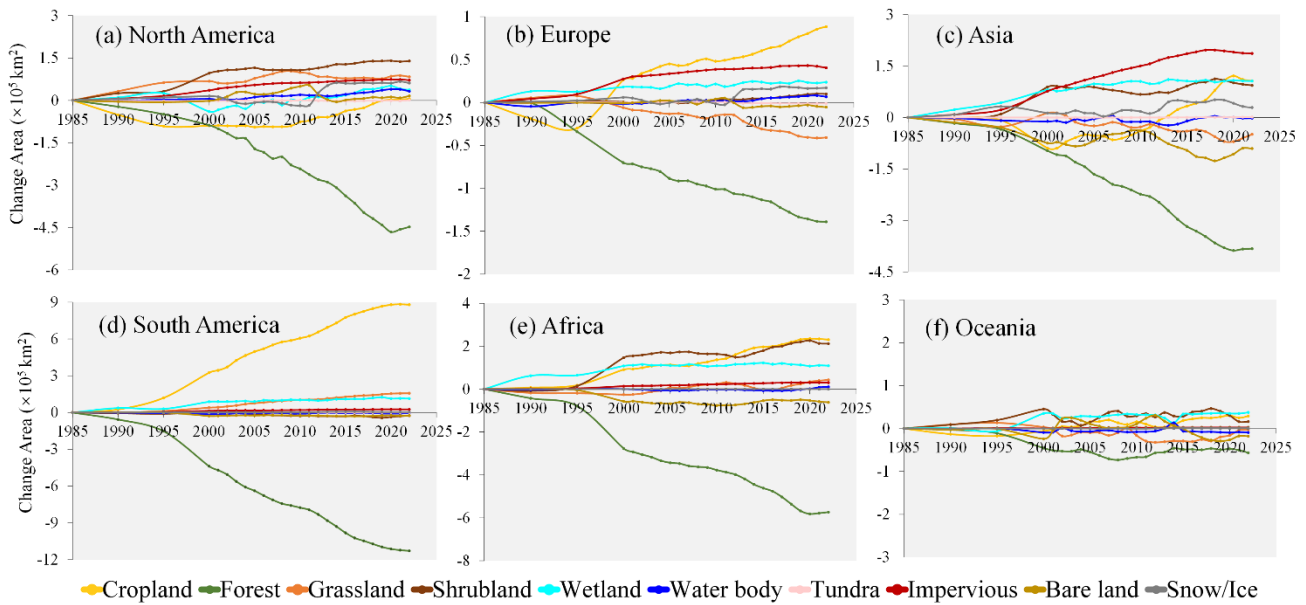


**Figure 5.** (a) The spatial distribution of global land-cover change intensity from 1985 to 2022 after aggregating to a resolution of 0.05°. (b) The net areas of 10 major land-cover types in GLC\_FCS30D from 1985 to 2022.

445 Figure 6 further analyzes the net area variations of 10 major land-cover types on six continents. The six continents exhibit various land-cover change characteristics, for example, steady forest loss and cropland gain dominate land-cover change in South America, while the net area variations of most land-cover types fluctuate in Australia. North America experiences obvious deforestation, and the forest loss area reaches approximately  $4.5 \times 10^5 \text{ km}^2$ . In contrast, shrubland, grassland, and impervious surface land-cover types show an overall increasing trend, with increases of  $1.4 \times 10^5 \text{ km}^2$ ,  $0.8 \times 10^5 \text{ km}^2$ , and  $0.72 \times 10^5 \text{ km}^2$ , respectively. Similarly, [Xian et al. \(2022\)](#) reported that forest losses and shrubland, grassland, and impervious surface gains are the dominant characteristics of the CONUS from 1985 to 2017. In Europe, the forest area continues to decrease, and the cropland area first decreased and then increased because of the collapse of the Soviet Union in 1990s. Abandoned croplands were transformed into pasture (which also belongs to the cropland land-cover type in the GLC\_FCS30D). In Asia, the increase in impervious surface is the most significant across the six continents with a net increase of  $1.9 \times 10^5 \text{ km}^2$ ; wetland also shows a large increase of  $1.1 \times 10^5 \text{ km}^2$ . The increased wetland

460 coverage comes from the increase in seasonal water bodies. South America and Africa experience similar land-cover change characteristics, with the most intense deforestation rates and the most significant increases in cropland. According to our statistics, the forest loss on these two continents amounts to  $16.9 \times 10^5 \text{ km}^2$  and the corresponding increase of cropland is approximately  $11.1 \times 10^5 \text{ km}^2$ . Last, because Oceania is more sensitive to climate change, especially in terms of precipitation, the fluctuations of shrubland, grassland, and bare land are evident because the conversion relationship between the three land-cover types is related to annual precipitation.

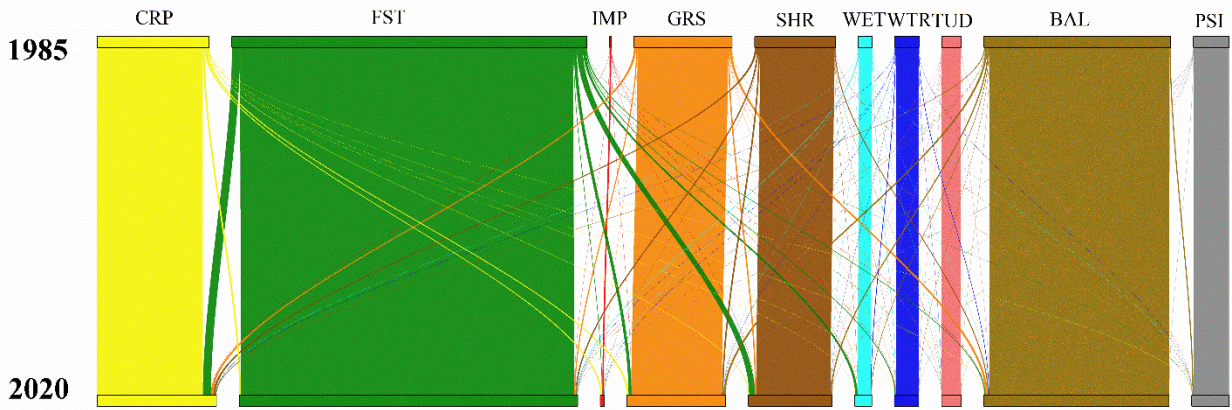


465 **Figure 6.** The net area variations of 10 major land-cover types on six continents from 1985 to 2022.

470 Figure 7 displays the land-cover transformation relationships from 1985 to 2022 in the GLC\_FCS30D dataset using Sankey diagrams. Global cropland and forest have obvious area changes and area proportions have changed from 12.08% and 38.26% in 1985 to 12.86% and 36.48% in 2022. Shrubland changed from 8.70% in 1985 to 9.03% in 2022. We mainly focus on forest, cropland, shrubland and impervious surface changes, which dominate the land-cover changes in Figure 5. There are three main causes of forest loss over the past 37 years: 1) 37.58% of deforested land was converted to cropland, which was more significant in tropical rainforest areas (Figure 8a); 2) 26.92% of the lost forest was regrown as shrubland, which is more common in mountainous areas affected by wildfires; and 3) 13.49% of deforested land was converted to grassland. Cropland is converted to forest, grassland, and impervious surface. A total of 26.29% of lost cropland is converted to grassland due to abandonment, 25.88% of lost cropland is covered by forests, and 21.01% of lost cropland resulted from urbanization. Lastly, regarding impervious surface, our primary focus was on identifying the sources contributing to its expansion. Our findings indicate that approximately 36.24% of the impervious surface increase can be attributed to the conversion of cropland, while 13.49% of the increase is a result of deforestation.

475





480 **Figure 7.** Sankey diagrams of the global land-cover changes during 1985-2022 in the GLC\_FCS30D dataset.

To visually understand the land-cover change process captured by the GLC\_FCS30D dataset over past 37 years, Figure 8 displays ~~two~~three typical enlargements (spatial location illustrated as two black rectangles in Figure 5a) of the Amazon rainforest (which experienced significant deforestation) and China's Yangtze River Delta (which underwent rapid urbanization) and Yellow River Delta (evident land-cover changes over coastal regions). These ~~two~~three typical areas experienced drastic land-cover changes and the GLC\_FCS30D accurately captures the spatiotemporal changes. ~~In specific~~Specifically, the deforestation in South America is widely recognized, and the GLC\_FCS30D clearly reflects this trend. Namely, the early deforestation showed a grid distribution, and then each grid gradually extended outward and finally connected into patches. The GLC\_FCS30D also shows that deforestation has not stopped in the region in terms of the rate of forest loss, and these findings are in line with the results of earlier researches ([Harris et al., 2021](#); [Potapov et al., 2022](#)). In the Yangtze River Delta, GLC\_FCS30D depicts that the dominant land-cover change over the enlargement is urbanization, and a large quantity of irrigated cropland has been converted to impervious surfaces. Meanwhile, urban expansion was significantly faster before 2010 than after 2010 with the GLC\_FCS30D. Lastly, the Yellow River Delta, as one of the typical coastal region, was selected to understand the GLC\_FCS30D for capturing these coastal land-cover changes. Obviously, the land-cover changes in the GLC\_FCS30D can be concluded into three aspects: 1) a large amount of flooded flats and flat flats were reclaimed as the aquaculture ponds, especially after 2000; 2) the mouth of the Yellow River turned from south to north (black rectangle), that is, there were large land-cover changes between tidal/flooded flats, water bodies and salt marshes; 3) a lot of impervious surfaces encroached the coastal water-bodies and flats. In short, if we combine real time-series remote-sensing observation data, the GLC\_FCS30D effectively captures the spatiotemporal changes of the land surface.

485

490

495

500

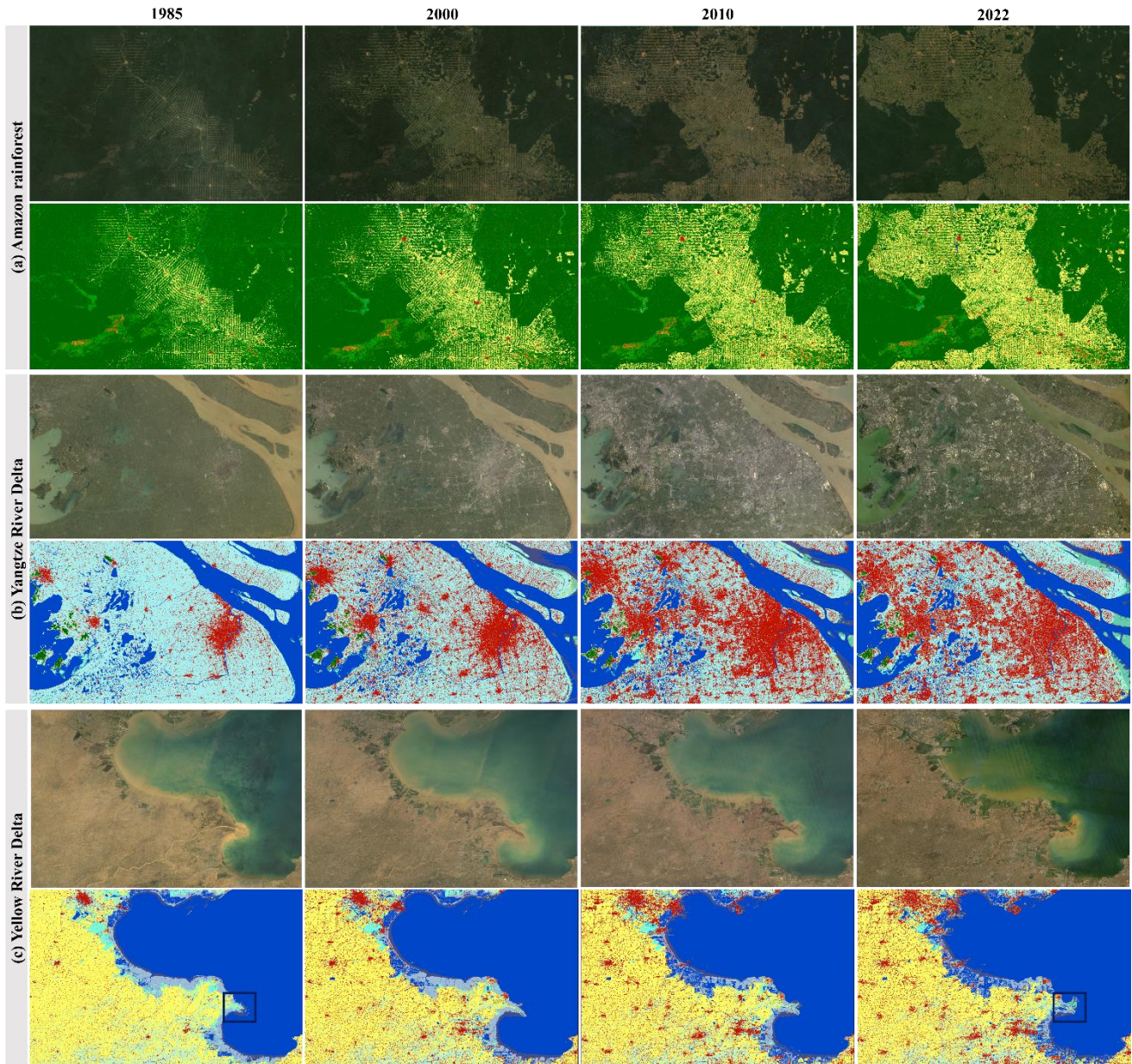


**Figure 8.** ~~Two~~Three typical enlargements of land-cover changes in the GLC\_FCS30D from 1985 to 2022 in (a) the Amazon rainforest, (b) the Yangtze River Delta in China, and (c) the Yellow River Delta in China. The color-coded legend is like the global map in Figure 4. In each case, the natural-color imagery from 1985 to 2022 is a composite taken from Landsat imagery.

#### 4.2 Accuracy assessment of the GLC\_FCS30D in 2020

Table 2 provides the error matrix and accuracy metrics for the GLC\_FCS30D dataset in the level-0 classification system containing 10 major land-cover types. The novel GLC\_FCS30D dataset attained an overall accuracy O.A. of 80.88% ( $\pm 0.27\%$ ). The cropland, forest, impervious surface, water body, as well as permanent snow and ice perform better in terms of the P.A. and U.A. than the remaining land-cover types, with corresponding accuracies exceeding 85%. The impervious surface and wetland datasets are independently generated and then overlaid on the GLC\_FCS30D, helping these complicated land-cover types achieve high accuracy metrics. Conversely, grassland, shrubland, and tundra have lower accuracies; for example, grassland

515 had the lowest P.A. of 54.41% and shrubland had the lowest U.A. of 57.63%. The two reasons that they performed poorly were as follows: 1) these land-cover types usually reflected heterogeneous and varied spectral and spatial characteristics, such as the grassland shared similar spectra with cropland and sparse shrubland in the growing season and mimicked bare-land features in harvest season; 2) all of them were distributed in climate-transition areas with complicated climate variations and landscapes.

520 **Table 2.** Error matrix of the GLC\_FCS30D dataset in 2020 based on the level-0 basic classification system. The reported Producer's Accuracy (P.A.) and User's Accuracy (U.A.) come with their corresponding standard errors (SE) shown in parentheses.

Reference	Map										Total	P.A.(SE)
	CRP	FST	GRS	SHR	WET	WTR	TUD	IMP	BAL	PSI		
	<b>O.A. = 80.88% (<math>\pm 0.27\%</math>)</b>											
CRP	15.442	0.792	0.679	0.388	0.086	0.027	0	0.174	0.117	0	17.704	87.22(0.54)
FST	0.513	28.712	0.315	0.811	0.371	0.021	0.008	0.063	0.113	0.002	30.93	<b>92.83(0.31)</b>
GRS	1.035	1.166	5.906	1.181	0.231	0.011	0.084	0.051	1.181	0.01	10.855	<b>54.41(1.02)</b>
SHR	0.555	1.798	0.863	5.392	0.161	0.013	0.019	0.05	0.502	0.002	9.356	<b>57.63(1.09)</b>
WET	0.068	0.465	0.156	0.157	4.047	0.347	0.031	0.021	0.222	0.001	5.516	73.37(1.27)
WTR	0.04	0.086	0.019	0.017	0.302	3.305	0.008	0.012	0.039	0.002	3.831	86.28(1.12)
TUD	0.01	0.123	0.168	0.167	0.018	0.03	2.444	0.002	0.473	0.02	3.454	70.76(1.65)
IMP	0.084	0.058	0.024	0.04	0.001	0.006	0.002	5.043	0.024	0	5.283	95.45(0.61)
BAL	0.13	0.049	0.783	0.585	0.043	0.045	0.577	0.048	9.239	0.131	11.628	79.45(0.8)
PSI	0	0.004	0.03	0.005	0	0.023	0.001	0	0.03	1.351	1.443	93.63(1.38)
Total	17.877	33.251	8.943	8.743	5.259	3.828	3.176	5.464	11.94	1.52		
U.A.(SE)	86.38 (0.55)	86.35 (0.4)	66.05 (1.07)	61.68 (1.11)	76.96 (1.2)	86.33 (1.35)	76.97 (1.6)	92.29 (0.77)	77.38 (0.82)	88.89 (1.72)		

Note: The abbreviations correspond to the 10 categories of the basic classification system in Table 1.

525 Table 3 provides the error matrix of the GLC\_FCS30D in 2020 in the LCCS level-1 validation system with 17 land-cover types. The GLC\_FCS30D-2020 dataset achieves an ~~overall accuracy~~ **O.A.** of 73.2404% ( $\pm 0.30\%$ ), which is lower than that in the level-0 classification system, because these similar land-cover subcategories more easily suffer from misclassifications. For example, forest has a P.A. of 92.83% ( $\pm 0.31\%$ ) and the P.A. rapidly decreases to the range of 58.29% ( $\pm 1.53\%$ ) to 82.39% ( $\pm 0.98\%$ ) when split into five fine subcategories. Cropland, forest, and bare land, which are further divided into multiple subcategories, show obvious decreases in accuracy over their subcategories in terms of P.A. and U.A. Taking cropland and forest as examples, approximately 31.7% of irrigated cropland (ICP) is misclassified as rainfed cropland (RCP) and so the U.A. of ICP is only 59.92%. More than 53.8% of mixture forests (MFT) are wrongly labeled as the other four forest subcategories and so the mixture forests have the lowest U.A. of 39.34% ( $\pm 1.38\%$ ). Meanwhile, sparse vegetation has the second lowest U.A. of 50.63% ( $\pm 1.47\%$ ) because of the confusion among sparse vegetation, grassland, and bare land. In the level-0 basic classification system (Table 1), sparse vegetation is grouped in with bare land. A previous study in Europe Union proposed grouping it as grassland (Gao et al., 2020). Wetland is further divided into coastal wetland (CWL) and inland wetland (IWL) in Table 3, and the CWL has higher U.A. than that of wetland in Table 2, primarily attributed to its significantly more accurate classification in the CWL (Zhang et al., 2023).

540

**Table 3.** Error matrix of the GLC\_FCS30D dataset in 2020 based on the LCCS level-1 validation system. The reported Producer's Accuracy (P.A.) and User's Accuracy (U.A.) come with their corresponding standard errors (SE) shown in parentheses.

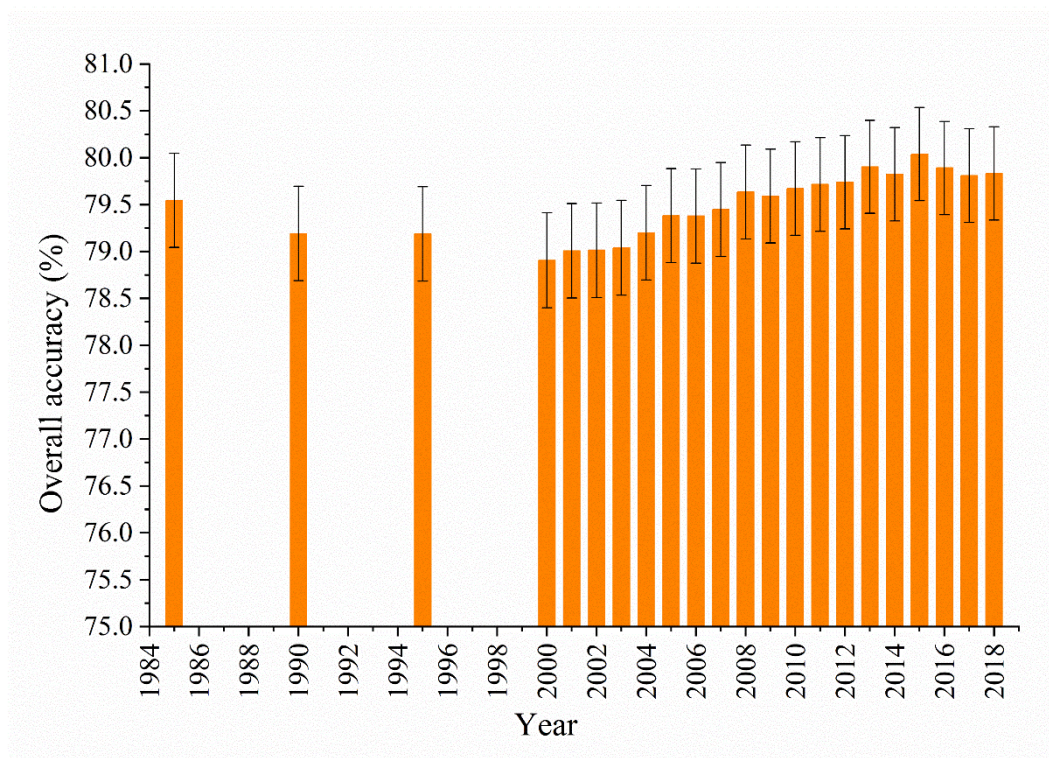
Reference	RCP	ICP	EBF	DBF	ENF	DNF	MFT	SHR	GRS	LMS	SVG	IWL	CWL	IMP	BAL	WTR	PSI	Total	P.A. (SE)
RCP	12.225	<b>1.023</b>	0.239	0.358	0.102	0.016	0.009	0.382	0.66	0	0.078	0.056	0.005	0.124	0.028	0.001	0	15.332	79.7(0.7)
ICP	0.397	1.932	0.026	0.016	0.005	0	0	0.01	0.025	0	0.012	0.029	0.005	0.052	0	0.018	0	2.527	76.45(1.81)
EBF	0.2	0.048	9.091	1.098	0.262	0.103	<b>0.151</b>	0.371	0.084	0	0.012	0.136	0.028	0.029	0.001	0.004	0	11.514	78.96(0.82)
DBF	0.187	0.016	0.632	6.838	0.537	0.294	<b>0.396</b>	0.235	0.144	0.002	0.019	0.077	0.002	0.025	0.005	0.004	0.002	9.054	75.53(0.97)
ENF	0.046	0.004	0.174	0.316	5.681	0.328	<b>0.439</b>	0.128	0.034	0.006	0.043	0.094	0	0.008	0.01	0.01	0	6.895	<b>82.39(0.98)</b>
DNF	0.008	0	0.002	0.13	0.245	1.854	<b>0.073</b>	0.071	0.053	0	0.011	0.025	0	0.001	0.007	0.002	0	2.414	76.79(1.85)
MFT	0.004	0	<b>0.019</b>	<b>0.176</b>	<b>0.234</b>	<b>0.013</b>	<b>0.828</b>	0.014	0.004	0	0	0.010	0.05	0	0.001	0	0	1.308	<b>58.29(1.53)</b>
SHR	0.518	0.042	0.299	0.9	0.328	0.131	0.034	5.44	0.871	0.019	0.441	0.157	0.005	0.05	0.065	0.013	0.002	9.438	57.63(1.09)
GRS	0.947	0.097	0.167	0.582	0.209	0.154	0.024	1.191	5.958	0.085	0.974	0.229	0.006	0.052	0.217	0.008	0.01	10.95	54.41(1.02)
LMS	0.006	0.004	0.001	0.022	0.044	0.053	0.001	0.168	0.169	2.465	0.379	0.02	0.001	0.002	0.098	0.026	0.02	3.484	70.76(1.65)
SVG	0.064	0.01	0.008	0.006	0.007	0.01	0.001	0.397	0.462	0.025	2.71	0.012	0	0.013	0.643	0.002	0.024	4.399	61.6(1.57)
IWL	0.01	0.002	0.044	0.029	0.103	0.022	0.002	0.048	0.017	0.008	0.042	2.673	0.024	0.001	0.012	0.224	0	3.263	<b>81.91(1.45)</b>
CWL	0.004	0.002	0.008	0.002	0.004	0.002	0.004	0.008	0.006	0	0.008	0.188	1.476	0.007	0.007	0.059	0	1.783	<b>82.77(1.92)</b>
IMP	0.074	0.011	0.008	0.008	0.037	0.002	0	0.041	0.024	0.002	0.014	0.004	0	5.087	0.01	0.004	0	5.329	95.45(0.61)
BAL	0.048	0.01	0.002	0.004	0.002	0.001	0	0.193	0.328	0.557	0.582	0.043	0.002	0.035	5.384	0.029	0.108	7.33	73.45(1.11)
WTR	0.014	0.024	0.014	0.014	0.019	0.008	0.006	0.011	0.016	0.007	0.011	0.168	0.114	0.011	0.019	3.054	0.002	3.509	87.04(1.22)
PSI	0	0	0	0.001	0.002	0	0	0.005	0.03	0.001	0.011	0	0	0	0.019	0.023	1.363	1.455	93.65(1.37)
Total	14.757	3.224	10.753	10.56	7.833	3.724	1.97	8.711	8.883	3.179	5.353	3.927	1.668	5.497	6.526	3.482	1.532		
U.A. (SE)	82.85 (0.67)	<b>59.92</b> <b>(1.85)</b>	84.55 (1.75)	64.76 (1)	72.52 (1.08)	49.77 (1.76)	<b>39.34</b> <b>(1.38)</b>	62.44 (1.11)	67.07 (1.07)	77.55 (1.59)	<b>50.63</b> <b>(1.47)</b>	<b>68.07</b> <b>(1.6)</b>	<b>88.49</b> <b>(1.68)</b>	92.54 (0.76)	82.5 (1.01)	87.73 (1.19)	88.96 (1.72)		
O.A.	<b>73.04% (±0.30%)</b>																		

Note: The abbreviations correspond to the 17 categories of the LCCS validation system in Table 1.

## 500 4.3 Accuracy assessment based on two third-party regional validation datasets

### 4.3.1 Time-series accuracy metrics of GLC\_FCS30D from LCMAP\_Val dataset

505 Figure 9 displays time-series variations of the overall accuracy of the GLC\_FCS30D dataset using the LCMAP\_Val annual validation dataset from 1985 to 2018 over the CONUS. The GLC\_FCS30D achieves a mean overall accuracy O.A. of 79.50% ( $\pm 0.50\%$ ) and varies from a high value of 80.04% ( $\pm 0.49\%$ ) in 2015 to a low value of 78.91% ( $\pm 0.51\%$ ) in 2000. The overall accuracy of GLC\_FCS30D is slightly lower at the early stage, which might be related to the density of Landsat observations. The early Landsat missions had weaker satellite-to-ground transmission and onboard recording capabilities (Roy et al., 2014a), so phenological variability and land-cover changes were more difficult to capture in the early stage.



510 **Figure 9.** The time-series overall accuracy of the GLC\_FCS30D dataset using the LCMAP\_Val annual reference dataset across the contiguous United States (CONUS) from 1985 to 2018. The error bars on the graph show the uncertainty of each data point.

515 Figure 10 further illustrates the time-series variations of P.A. and U.A. for the GLC\_FCS30D dataset in the CONUS. Visually, the P.A. and U.A. of 10 major land-cover types range from 45% to 100% and 35% to 100%, respectively, and the time-series variations are stable. Among them, the water body land-cover type has the highest accuracy metrics, achieving mean P.A. and U.A. values of 95.31% ( $\pm 1.14\%$ ) and 98.53% ( $\pm 0.66\%$ ), respectively, which benefit from its unique spectral characteristics. Cropland follows with mean P.A. and U.A. values of 93.37% ( $\pm 0.74\%$ ) and 87.70% ( $\pm 0.94\%$ ), respectively. Forest ranks third with a high P.A. of 97.75% ( $\pm 0.35\%$ ) but relatively low U.A. of 82.42% ( $\pm 0.82\%$ ); the unbalanced metrics are because GLC\_FCS30D and LCMAP\_Val have different definitions for forest. GLC\_FCS30D defines the tree cover of the forest as greater than 15% and the threshold setting of LCMAP\_Val is 10%, so many shrublands in the GLC\_FCS30D are labeled as forest in the LCMAP\_Val. Wetland has a U.A. value of 90.47% ( $\pm 2.05\%$ ) but a

520

P.A. value of 57.07% ( $\pm 2.75\%$ ), which is also caused by a discrepancy in the definition of wetland. GLC\_FCS30D identifies seasonal water bodies as wetland while the LCMAP\_Val classifies them as water body.

525 Impervious surface has a P.A. lower than 60% mainly because the GLC\_FCS30D and LCMAP\_Val datasets have different definitions of impervious surface. LCMAP\_Val defines buildings and the surrounding green areas as developed, while GLC\_FCS30D only includes the artificial buildings (houses, roads, squares, and so on).

530 Bare land and shrubland have the lowest U.A. values of 35.58% ( $\pm 4.39\%$ ) and 47.29% ( $\pm 1.56\%$ ), respectively, mainly because both of them are easily confused with grassland due to the complicated spectral characteristics and coexist in climate-sensitive semi-arid regions (e.g., the Midwestern United States). [Xian et al. \(2022\)](#) emphasized that long-term monitoring of shrubs and grasslands presents significant challenges in the CONUS. Permanent snow and ice, which is sparsely distributed in high-elevation mountainous areas of the United States, has unique and specific spectral characteristics, so it achieves 100% P.A. in the GLC\_FCS30D. The large fluctuations in U.A. are because the LCMAP\_Val dataset has a small sample size for ice and snow and the

535 commission error of other land-cover types causes large variations.

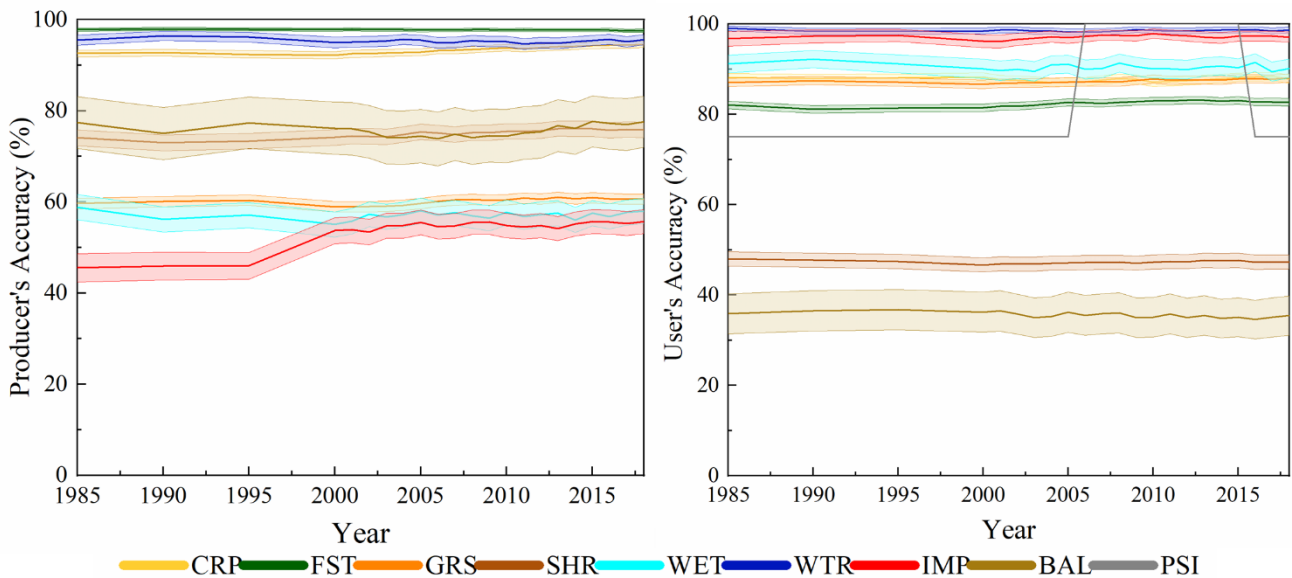
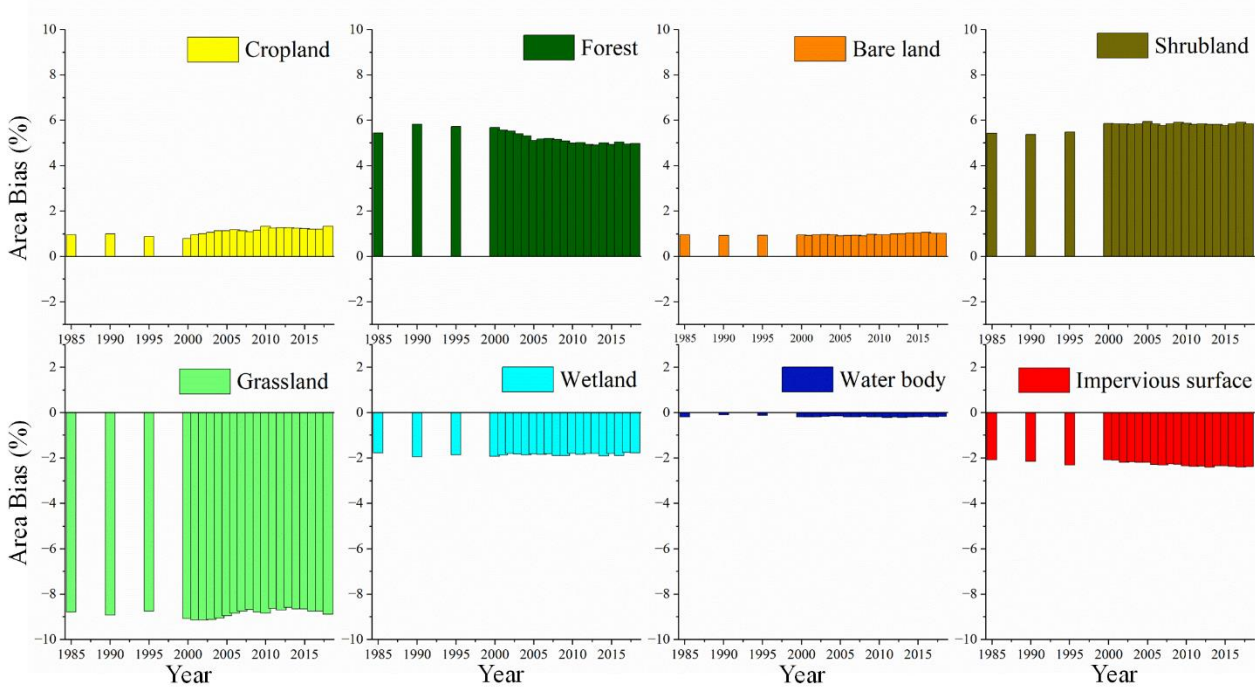


**Figure 10.** The time-series producer's accuracy and user's accuracy of GLC\_FCS30D based on the LCMAP\_Val dataset from 1985 to 2018 in the contiguous United States (CONUS). The error band represents  $\pm 1$  standard errors.

540 Figure 11 indicates the area-bias percentage of eight land-cover types estimated by GLC\_FCS30D and LCMAP\_Val across the CONUS. Intuitively, the GLC\_FCS30D and LCMAP\_Val share similar total areas for estimation of cropland, bare land, and water body, and show evident area deviations for estimating forest, shrubland, and grassland. The deviations in shrubland and grassland are mainly because these land-cover types coexist in the semi-arid regions of the central United States and share similar spectral characteristics and temporal variability; thus, some grasslands in the LCMAP\_Val are considered as shrubland in the

545 GLC\_FCS30D. [Xian et al. \(2022\)](#) also failed to distinguish grassland and shrubland and combined them as a group in generating the LCMAP annual maps. The LCMAP\_Val has a broader definition of impervious surface and resulting negative bias, so the impervious surface area estimated in LCMAP\_Val is larger than the assessment in GLC\_FCS30D dataset.



550

**Figure 11.** The area-bias percentage of eight land-cover types in the GLC\_FCS30D and LCMAP\_Val datasets from 1985 to 2017 in the contiguous United States (CONUS).

555

Table 4 further analyzed the confusion matrix of land-cover changed and unchanged pixels in GLC FCS30D using LCMAP Val dataset. It should be noted that the land-cover changed samples in the LCMAP\_Val was still sparse, that is, the size of changed samples cannot support the land-cover change analysis over specific land-cover changes. Similarly, Stehman et al. (2021) also grouped the land-cover types into ‘No change’ and ‘change’ types for analyzing the land-cover changes. In this study, using the ‘changed’ and ‘unchanged’ validation points in LCMAP\_Val, the O.A. of the GLC FCS30D reached the  $90.49 \pm 0.45\%$ . In particular, the unchanged land-cover pixels played a dominant role and reached the high P.A. of 92.84% and U.A. of 96.28%. In contrast, the P.A. and U.A. of concerned land-cover changed pixels were  $72.26 \pm 2.04\%$  and  $56.62 \pm 2.00\%$ , and its F1 score was 63.49%.

560

**Table 4.** The confusion matrix of changed and unchanged pixels in GLC FCS30D using LCMAP\_Val datasets.

	Unchanged	Changed	Total	P.A. (SE)	F1
Unchanged	82.21	6.34	88.55	92.84(0.42)	94.53
Changed	3.18	8.27	11.45	<b>72.26(2.04)</b>	63.49
Total	85.39	14.61			
U.A. (SE)	96.28(0.32)	<b>56.62(2.00)</b>			
O.A. (SE)			90.49(0.45)		

#### 4.3.2 Time-series accuracy metrics of GLC\_FCS30D from the LUCAS dataset

565

Table 4-5 lists the time-series accuracy metrics of the GLC\_FCS30D dataset across the European Union (EU) from 2006 to 2018 using the LUCAS dataset. The GLC\_FCS30D dataset has a mean O.A. overall accuracy of 81.91% ( $\pm 0.09\%$ ) ranging from 81.64% (0.09%) to 82.11% (0.09%) in EU. The two dominant land-cover types (cropland and forest) that cover almost 70% of the entire EU area (Gao et al., 2020) have higher P.A. and

U.A. values than other land-cover types. The P.A. and U.A. of cropland exceed 85% and 93%, respectively. Forest has unbalanced P.A. (approximately 95%) and U.A. values (approximately 76%) because the LUCAS dataset defines forest more broadly than the GLC\_FCS30D dataset. In [particulars specific](#), sparse vegetation associated with forest is grouped as forest in LUCAS but as bare land in GLC\_FCS30D. [Gao et al. \(2020\)](#) explained the discrepancy in the forest definition between LUCAS and GLC\_FCS30. Shrubland, grassland, and bare land showed inferior performance in both P.A. and U.A. because of their complicated spectral variability and spatial heterogeneity. [Gao et al. \(2020\)](#) also found that three global 30-m land-cover products (GlobeLand30, FROM\_GLC, and GLC\_FCS30) exhibited poor performance for these three land-cover types. Urban green space and discontinuous urban fabric, excluding from the GLC\_FCS30D, are grouped as impervious surface in the LUCAS. Thus, the impervious surface also has a low P.A. of approximately 59%. Last, we further investigate the temporal variability of P.A. and U.A. and find that permanent ice and snow and wetland show greater variability and that both are closely related to annual temperature and precipitation; namely, their spatial distributions are affected by the natural environment.

**Table 45.** Time-series accuracy metrics of the GLC\_FCS30D dataset using the LUCAS validation dataset across the European Union.

	2006		2009		2012		2015		2018	
	P.A.(SE)	U.A.(SE)	P.A.(SE)	U.A.(SE)	P.A.(SE)	U.A.(SE)	P.A.(SE)	U.A.(SE)	P.A.(SE)	U.A.(SE)
CRP	85.49(0.11)	93.37(0.08)	85.40(0.11)	93.31(0.08)	85.50(0.11)	93.17(0.08)	85.47(0.11)	93.05(0.08)	85.52(0.11)	92.82(0.08)
FST	95.22(0.08)	76.71(0.15)	94.97(0.08)	76.71(0.15)	94.79(0.09)	76.82(0.15)	94.36(0.09)	76.82(0.15)	93.71(0.09)	76.85(0.15)
GRS	6.13(0.26)	21.31(0.83)	6.10(0.26)	21.13(0.83)	6.05(0.26)	20.98(0.83)	6.08(0.26)	20.71(0.82)	5.99(0.26)	20.74(0.82)
SHR	8.13(0.42)	8.93(0.46)	8.25(0.43)	8.92(0.46)	8.02(0.42)	8.77(0.46)	7.84(0.42)	8.60(0.45)	8.35(0.43)	8.96(0.46)
WET	63.10(0.81)	66.55(0.81)	61.40(0.81)	65.55(0.82)	61.86(0.81)	66.21(0.82)	62.64(0.81)	66.60(0.81)	62.94(0.81)	65.34(0.81)
WTR	89.73(0.40)	92.44(0.36)	90.09(0.40)	92.53(0.35)	90.28(0.39)	92.36(0.36)	90.83(0.38)	91.63(0.37)	90.10(0.40)	91.56(0.37)
IMP	58.55(0.56)	72.69(0.56)	59.21(0.55)	72.06(0.56)	59.06(0.55)	71.72(0.56)	58.65(0.55)	70.85(0.56)	59.01(0.55)	70.29(0.56)
BAL	52.77(1.12)	39.62(0.95)	52.90(1.12)	38.44(0.93)	52.19(1.13)	37.70(0.93)	52.07(1.13)	36.16(0.90)	52.33(1.13)	34.69(0.87)
PSI	86.02(5.00)	35.01(4.38)	91.40(4.04)	36.56(4.38)	89.25(4.46)	31.86(4.00)	96.24(2.74)	31.40(3.81)	96.24(2.74)	31.35(3.81)
O.A.(SE)	82.11(0.09)		81.99(0.09)		81.97(0.09)		81.82(0.09)		81.64(0.09)	

Table 5-6 shows the area proportions of 10 major land-cover types from the GLC\_FCS30D dataset (Map) and LUCAS validation dataset (Ref), respectively. The area bias (AB) measures the area deviations of the two different datasets for the same land-cover type. Overall, the GLC\_FCS30D overestimates the total area assessments of forest, bare land, and ice and snow, and underestimates the remaining land-cover types in comparison to the LUCAS estimations. In particular, the AB of forest is the most significant overestimation of +7.356%, and the underestimated MB of cropland is -4.086%. Cropland and forest cover together account for approximately 70% of the total EU area ([Gao et al., 2020](#)), as a result, the area bias (AB) values for these two land-cover types are more noticeable or pronounced compared to the AB values of the other land-cover types.

**Table 56.** The area proportions and area bias (AB) values of 10 major land-cover types from the GLC\_FCS30D dataset (Map) and the LUCAS validation dataset (Ref).

	2006			2009			2012			2015			2018		
	Map	Ref	AB	Map	Ref	AB	Map	Ref	AB	Map	Ref	AB	Map	Ref	AB
CRP	46.48	50.62	-4.14	46.46	50.64	-4.18	46.59	50.67	-4.08	46.63	50.69	-4.06	46.77	50.74	-3.97



FST	41.39	33.76	7.63	41.28	33.75	7.53	41.14	33.73	7.41	40.96	33.73	7.23	40.66	33.68	6.98
GRS	1.21	4.15	-2.94	1.21	4.15	-2.94	1.21	4.15	-2.94	1.23	4.15	-2.92	1.21	4.15	-2.94
SHR	1.91	2.08	-0.17	1.94	2.08	-0.14	1.92	2.08	-0.16	1.91	2.07	-0.16	1.95	2.06	-0.11
WET	1.70	1.75	-0.05	1.68	1.74	-0.06	1.68	1.73	-0.05	1.69	1.71	-0.02	1.73	1.72	0.01
WTR	2.75	2.85	-0.1	2.76	2.85	-0.09	2.77	2.85	-0.08	2.81	2.85	-0.04	2.79	2.86	-0.07
IMP	3.18	3.82	-0.64	3.25	3.83	-0.58	3.25	3.82	-0.57	3.27	3.82	-0.55	3.32	3.82	-0.5
BAL	1.32	0.95	0.37	1.36	0.95	0.41	1.37	0.95	0.42	1.42	0.95	0.47	1.49	0.95	0.54
PSI	0.06	0.02	0.04	0.06	0.02	0.04	0.07	0.02	0.05	0.07	0.02	0.05	0.07	0.02	0.05

Table 7 presented the confusion matrix of changed and unchanged pixels using the LUCAS validation datasets. The O.A. of the GLC\_FCS30D reached  $90.36 \pm 0.38\%$ , the P.A. and U.A. of the changed pixels were  $52.86 \pm 2.04\%$  and  $73.31 \pm 2.00\%$ , and the corresponding F1 score was 61.43%. In contrast, the unchanged land-cover pixels reached the high P.A. and U.A., and both two metrics exceeded 90%. Thus, the changed land-cover pixels were more difficult to capture comparing with these unchanged pixels. Similarly, Stehman et al. (2021) also found that the accuracy metrics of changed pixels were greatly lower than that of unchanged pixel, the producer's accuracy of changed pixels and unchanged pixels were 16% and 99%, respectively.

**Table 7.** The confusion matrix of changed and unchanged pixels in GLC\_FCS30D using time-series LUCAS datasets across the Europe Union.

	Unchanged	Changed	Total	P.A. (SE)	F1
Unchanged	82.69	2.79	85.48	96.73	94.49
Changed	6.84	7.68	14.52	52.86	61.43
Total	89.53	10.47			
U.A. (SE)	92.36(0.36)	73.31(1.74)			
O.A. (SE)	90.36(0.38)				

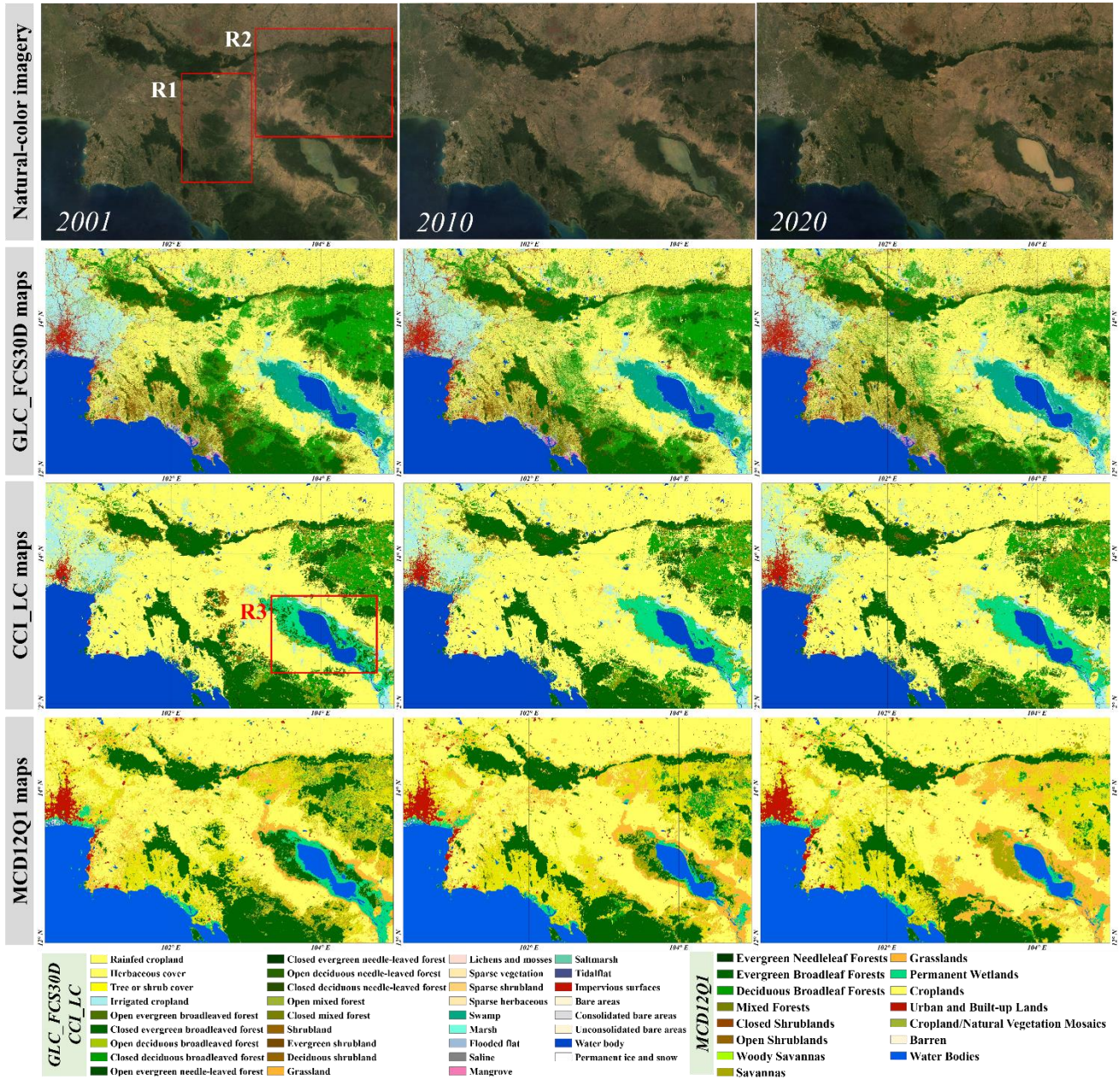
#### 4.4 The comparisons with other global land-cover dynamic products

Figure 12 gave the qualitative comparisons between our GLC\_FCS30D and two widely used land-cover dynamic datasets (CCI LC and MCD12Q1) during 2001-2020 in the Indo-China Peninsula, in which experienced evident land-cover changes in forest deforestation and urban expansion. In terms of the urban expansion, three datasets revealed the quick urbanization in the mega-city of Bangkok, and the CCI LC underestimated the impervious surface areas in 2001 comparing with two other datasets. Meanwhile, the GLC\_FCS30D also captured more spatial details (such as: rural building and road networks) than CCI LC and MCD12Q1 because of its high spatial resolution of 30 m.

In terms of the most significant deforestation, the CCI LC showed the worst performance because 1) it underestimated the forest covers in the 2001 (the rectangle region 1, R1), that is, some forests were wrongly labeled as the croplands; 2) some deforested forests cannot be captured during the period of 2001-2020 in rectangle region 2 (R2), so their deforested forest area was less than that of GLC\_FCS30D and MCD12Q1; and 3) there was obvious misclassification problem between forest and wetland in 2001 (the rectangle region 3, R3). Then, the MCD12Q1 also suffered the omission error for forest in R1, namely, the captured forest area in 2001 was lower than their actual areas based on the natural-color imagery. As for the evident deforestation in the R2, we can find that almost all forest pixels changed to the other land-cover types (savanna and grassland) in MCD12Q1, which was obviously deviated from the actual situation, thus, MCD12Q1 over-estimated the forest

620

deforestation. Meanwhile, the time-series MCD12Q1 showed various land-cover distributions in the R3, which indicated that the MCD12Q1 performed lower mapping accuracy and temporal stability for these wetland areas. In comparison, the GLC\_FCS30D achieved the best performance in capturing the spatial distribution of forest in 2001, forest deforestation during 2001-2020, and wetland stability.



625

Figure 12. The comparisons between GLC\_FCS30D with CCI\_LC and MCD12Q1 land-cover dynamic products in Indo-China Peninsula during 2001-2020. The natural-color imagery are composed from the time-series Landsat imagery.

630

Figure 13 showed another comparison example about three datasets in Paraguay, South America, and the most evident land-cover change was the deforestation and cropland incensement according to the time-series natural-color Landsat imagery. In terms of the spatial distribution, the consistency between GLC\_FCS30D and CCI\_LC was higher, while the MCD12Q1 was obviously different from the other two datasets. A large amount of deciduous broadleaved forests were labeled as the savanna and woody savanna, and most croplands were

identified as the grasslands in the MCD12Q1, which mainly because of the difference of classification system. Then, as for the land-cover change areas, the GLC\_FCS30D performed the highest accuracy and captured the richer spatial details. For example, the deforestation intensity during 2010-2020 was significantly greater than that during 2010-2020, and the GLC\_FCS30D also revealed the regular deforestation caused by human factors. In contrast, the CCI\_LC and MCD12Q1 failed to capture the deforestation during 2010-2020, and the small and fragmented changes (caused by human activities) also cannot be captured.

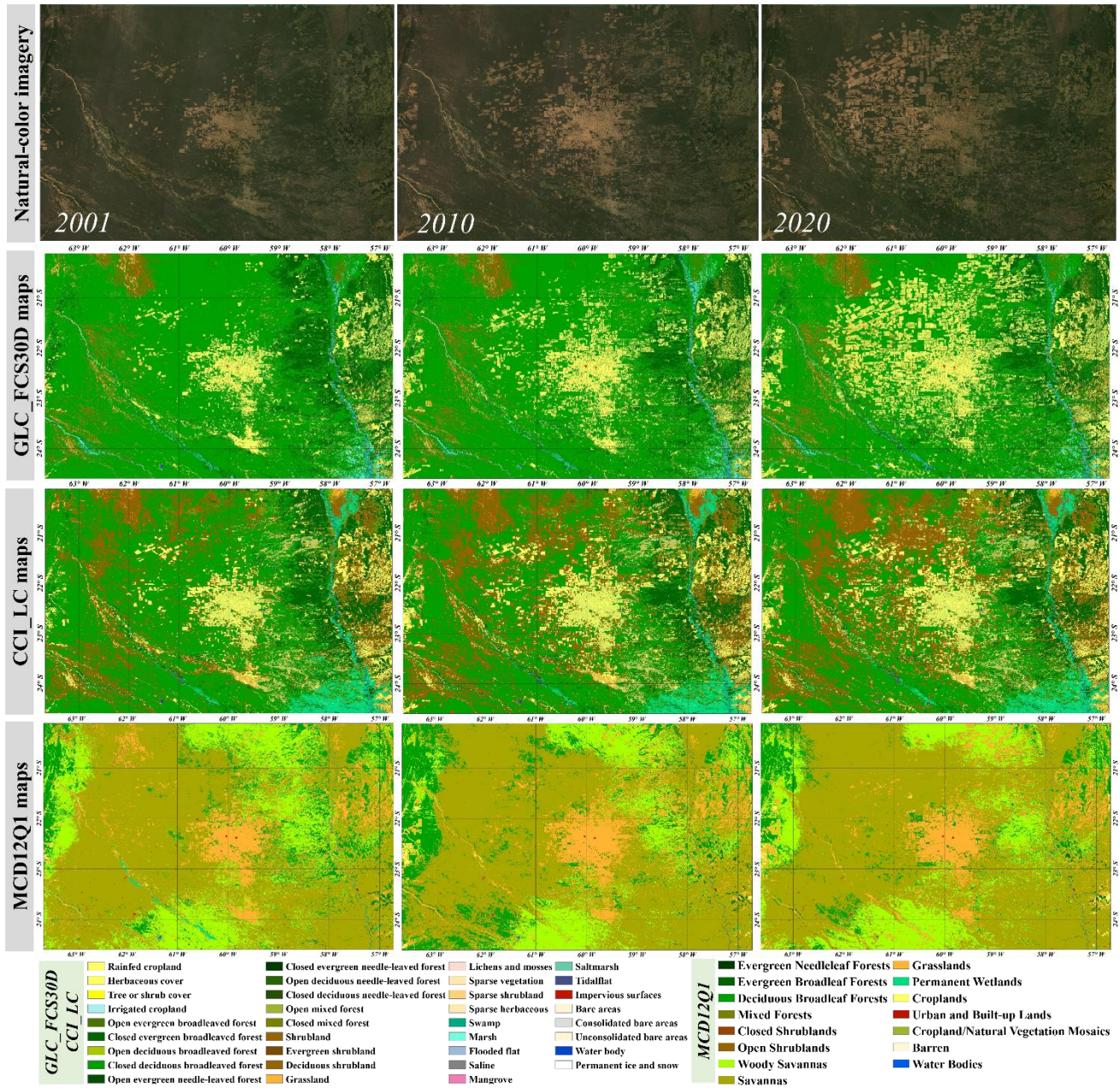


Figure 13. The comparisons between GLC\_FCS30D with two time-series land-cover dynamic datasets in Paraguay, South America, during 2001-2020.

#### 4.5 Limitations and perspectives of the GLC\_FCS30D dataset

To achieve the goal of accurate and robust monitoring of global land-cover change, four steps are adopted: 1) combining the advantages of the CCD model and full time-series Landsat observations to capture the land-

cover change time-points for any changed pixels; 2) using the temporally stable areas as prior knowledge to ensure the quality of training samples and adopting local adaptive modeling to update the land-cover transitions of these changed pixels; 3) independently developing global thematic products for two complicated land-cover types (impervious surface and wetland) to improve the reliability of the GLC\_FCS30D; and 4) applying the ‘spatiotemporal consistency checking’ optimization in Section 3.3.3 to further guarantee the stability and accuracy of the GLC\_FCS30D. The accuracy assessments, using the developed global validation dataset and two third-party datasets, demonstrate that the GLC\_FCS30D fulfills accuracy requirements at a baseline year and for time-series variability over global or national scales. Comparisons with other land-cover products also highlight the superiority of the GLC\_FCS30D in terms of classification system diversity and monitoring accuracy of these changed-areas. However, long time-series monitoring of global land-cover change is an extremely complex and difficult task ([Hansen and Loveland, 2012](#); [Song et al., 2018](#); [Winkler et al., 2021](#); [Xian et al., 2022](#)). Although this study takes a series of measurements and methods to achieve global 30-m land cover change monitoring over past 37 years, there are still some uncertainties and limitations that need to be resolved in further work.

The CCD algorithm makes full use of dense satellite observations to capture land-cover changes robustly and accurately ([Zhu and Woodcock, 2014b](#); [Zhu et al., 2012](#)). However, previous studies have demonstrated that their reliability is highly correlated to the density of valid satellite observations ([Bullock et al., 2022](#); [Ye et al., 2021](#); [Zhu et al., 2019](#)). Cloudy and snowy areas have greater uncertainty for capturing the time points of land-cover change ([DeVries et al., 2015](#); [Xian et al., 2022](#)). Additionally, due to the limited storage capacity and satellite-ground data-transmission capacity of early satellites, the density of Landsat imagery is sparse before 2000 (only Landsat 5 single-satellite acquired data) ([Roy et al., 2014b](#)). In this study, we combine the satellite observations from two years before and after the nominal center year from 1985 to 1995; for example, we update the land-cover maps in 1995 using all available imagery from 1993 to 1997. However, a previous study found that northeastern Asia did not have any valid Landsat observations before 2000 ([Zhang et al., 2022](#)), which means some land-cover changes could not be captured in the GLC\_FCS30D in these areas before 2000. To solve the problem of missing and sparse observations, a useful solution is to fuse multisourced remote-sensing imagery. For example, [Zhang et al. \(2021c\)](#) combined Landsat and Sentinel-2 imagery to track tropical forest disturbances with overall accuracy of more than 87%. Therefore, further work will investigate the feasibility of integrating Sentinel 1/2, MODIS, and AVHRR imagery as auxiliary datasets.

GLC\_FCS30D reveals a large number of land-cover changes in the semi-arid regions illustrated in Figure 5a, in which the land-cover changes are more influenced by climate factors. For example, the central region of Australia is a typical semi-arid region, and the dominant land-cover types are grassland, sparse vegetation, shrubland, and bare land. In general, if there is sufficient annual precipitation, the distributions of shrubland and grassland in the area will be more extensive; otherwise the area will be dominated by bare land and sparse vegetation ([Dong et al., 2020](#); [Ge et al., 2022](#)). Recently, some studies suggested suppressing these changes; for example, [Bastos et al. \(2022\)](#) chose to suppress these land-cover changes by fusing these four land-cover types into the single grassland land-cover type in Australia, and [Xian et al. \(2022\)](#) combined grassland and shrubland together in the CONUS. Whether these frequent and climate-sensitive land-cover changes should be suppressed will be considered in our further work.

Although we used a global validation dataset to assess the capability of GLC\_FCS30D in the baseline year of 2020 and two third-party regional datasets to assess its time-series accuracy variability in the European Union

685 and the CONUS, the accuracy assessment work should be strengthened. In particular~~specific~~, the classification system differences among GLC\_FCS30D, LUCAS, and LCMAP\_Val cannot be ignored. For example, the impervious surface land-cover type in the LUCAS and LCMAP\_Val contains artificial surfaces and their surroundings (such as city greenery) (Stehman et al., 2021; Xian et al., 2022), while the GLC\_FCS30D only includes artificial structures (Zhang et al., 2022), so the impervious surface in GLC\_FCS30D has low P.A. when  
690 validating with the LUCAS and LCMAP\_Val datasets in Section 4.3. The time-series accuracy variability is only analyzed in two regions, so its performance in more complex areas (such as Africa and Asia) needs to be further ~~studied~~investigated. Thus, our future work would ~~collect~~be paid on long-term time-series validation data sets for more regions and on building a long time-series global validation dataset based on the existing works in Section 2.5.1, and then analyzed the accuracy metrics of the land-cover changed pixels for all land-  
695 cover type and their intra-annual variability.

## 5. Data availability

The developed GLC\_FCS30D dataset can be freely accessible via <https://doi.org/10.5281/zenodo.8239305> (Liu et al., 2023). To allow users to better select this dataset, it is saved as 961 5° × 5° independent tiles. Each tile is named as ‘GLC\_FCS30D\_yyyyYYYY\_E/W\*\*N/S\*\*.tif’, in which ‘E/W\*\*N/S\*\*’ represents the  
700 longitude and latitude coordinates of the top-left corner, and yyyy and YYYY are the start and end years of the land-cover change monitoring. The GLC\_FCS30D contains 26 time-step maps from 1985 to 2022, updated every five years before 2000 and annually from 2000 to 2022. The first three time steps are saved together and the following 23 time steps are saved separately. For example, GLC\_FCS30D\_19851995\_E115N15.tif and GLC\_FCS30D\_20002022\_E115N15.tif are the first three time-steps and the following 23 annual time-steps  
705 data from 1985 to 2022 for the region of 115°–120°E, 10°–15°N, respectively.

## 6. Conclusion

Land cover change is the main cause or driving force of global climate change and has attracted increasing attention over the past decades. Long time-series global land-cover dynamic monitoring is still a challenging task. In this study, the first global 30-m land-cover dynamic dataset with fine classification system  
710 (GLC\_FCS30D), containing 35 fine land-cover sub-categories and covering the period of 1985 to 2022 with 26 time-steps, is generated on the GEE platform. In specific, we take advantage of the full time-series Landsat observations and the CCD algorithm to capture the time-points of changed areas, and then update and optimize the land-cover changed areas based on the local adaptive modeling strategy and a temporal-consistency algorithm. The accuracy assessments indicate that the proposed method can achieve accurate and spatiotemporally consistent land-cover change monitoring, and the GLC\_FCS30D achieves an overall accuracy  
715 in 2020 of 80.88% (±0.27%) for the basic classification system (10 major land-cover types) and 73.2404% (±0.30%) for the LCCS level-1 validation system (17 LCCS land-cover types). Therefore, the GLC\_FCS30D is the first global land-cover dynamic monitoring product with a 37-year time span and the most diverse classification system. It will be essential for sustainable development, environmental protection, and informed  
720 decision-making to address the challenges of a rapidly changing world.

## Financial support

This research has been supported by [the National Natural Science Foundation of China \(grant no. 41825002\)](#), the Open Research Program of the International Research Center of Big Data for Sustainable Development Goals (grant no. CBAS2022ORP03) and the National Natural Science Foundation of China (grant no. 42201499).

## Author contributions

LL and XZ conceptualized and investigated the project. XZ, TZ, XC designed the methodology, TZ, WL, HX and JW performed the validation. XZ prepared the original draft of the paper, LL and HX reviewed and edited the paper.

## Competing interests

The authors declare that they have no conflict of interest.

## References

Azzari, G. and Lobell, D. B.: Landsat-based classification in the cloud: An opportunity for a paradigm shift in land cover monitoring, *Remote Sensing of Environment*, 202, 64-74,

<https://doi.org/10.1016/j.rse.2017.05.025>, 2017.

Büttner, G. and Eiselt, B.: LUCAS and CORINE Land Cover. EEA and Eurostat Luxembourg, 2013.

Ballin, M., Barcaroli, G., Masselli, M., and Scarnò, M.: Redesign sample for land use/cover area frame survey (LUCAS) 2018, Eurostat: statistical working papers. doi, 10, 132365, 2018.

Ban, Y., Gong, P., and Giri, C.: Global land cover mapping using Earth observation satellite data: Recent progresses and challenges, *ISPRS Journal of Photogrammetry and Remote Sensing*, 103, 1-6,

<https://doi.org/10.1016/j.isprsjprs.2015.01.001>, 2015.

Bastos, A., Ciais, P., Sitch, S., Aragao, L., Chevallier, F., Fawcett, D., Rosan, T. M., Saunois, M., Gunther, D., Perugini, L., Robert, C., Deng, Z., Pongratz, J., Ganzenmuller, R., Fuchs, R., Winkler, K., Zaehle, S., and Albergel, C.: On the use of Earth Observation to support estimates of national greenhouse gas emissions and sinks for the Global stocktake process: lessons learned from ESA-CCI RECCAP2, *Carbon Balance Manag.*, 17, 15, <https://doi.org/10.1186/s13021-022-00214-w>, 2022.

Belgiu, M. and Drăguț, L.: Random forest in remote sensing: A review of applications and future directions, *ISPRS Journal of Photogrammetry and Remote Sensing*, 114, 24-31,

<https://doi.org/10.1016/j.isprsjprs.2016.01.011>, 2016.

Bullock, E. L., Healey, S. P., Yang, Z., Houborg, R., Gorelick, N., Tang, X., and Andrianirina, C.: Timeliness in forest change monitoring: A new assessment framework demonstrated using Sentinel-1 and a continuous change detection algorithm, *Remote Sensing of Environment*, 276, 113043,

<https://doi.org/10.1016/j.rse.2022.113043>, 2022.

Bullock, E. L., Woodcock, C. E., and Holden, C. E.: Improved change monitoring using an ensemble of time series algorithms, *Remote Sensing of Environment*, doi: 10.1016/j.rse.2019.04.018, 2019. 111165,

<https://doi.org/10.1016/j.rse.2019.04.018>, 2019.

- d'Andrimont, R., Yordanov, M., Martinez-Sanchez, L., Eiselt, B., Palmieri, A., Dominici, P., Gallego, J., Reuter, H. I., Joebges, C., and Lemoine, G.: Harmonised LUCAS in-situ land cover and use database for field surveys from 2006 to 2018 in the European Union, *Scientific data*, 7, 352, 2020.
- 760 Defourny, P., Kirches, G., Brockmann, C., Boettcher, M., Peters, M., Bontemps, S., Lamarche, C., Schlerf, M., and M., S.: Land Cover CCI: Product User Guide Version 2, 2018. 2018.
- DeVries, B., Verbesselt, J., Kooistra, L., and Herold, M.: Robust monitoring of small-scale forest disturbances in a tropical montane forest using Landsat time series, *Remote Sensing of Environment*, 161, 107-121, <https://doi.org/10.1016/j.rse.2015.02.012>, 2015.
- 765 Dong, J., Xiao, X., Kou, W., Qin, Y., Zhang, G., Li, L., Jin, C., Zhou, Y., Wang, J., Biradar, C., Liu, J., and Moore, B.: Tracking the dynamics of paddy rice planting area in 1986–2010 through time series Landsat images and phenology-based algorithms, *Remote Sensing of Environment*, 160, 99-113, <https://doi.org/10.1016/j.rse.2015.01.004>, 2015.
- Dong, S., Shang, Z., Gao, J., and Boone, R. B.: Enhancing sustainability of grassland ecosystems through ecological restoration and grazing management in an era of climate change on Qinghai-Tibetan Plateau, *Agriculture, Ecosystems & Environment*, 287, 106684, <https://doi.org/10.1016/j.agee.2019.106684>, 2020.
- 770 Du, P., Samat, A., Waske, B., Liu, S., and Li, Z.: Random Forest and Rotation Forest for fully polarized SAR image classification using polarimetric and spatial features, *Isprs Journal of Photogrammetry & Remote Sensing*, 105, 38-53, <https://doi.org/10.1016/j.isprsjprs.2015.03.002>, 2015.
- 775 Foley, J. A., Defries, R., Asner, G. P., Barford, C., Bonan, G., Carpenter, S. R., Chapin, F. S., Coe, M. T., Daily, G. C., Gibbs, H. K., Helkowski, J. H., Holloway, T., Howard, E. A., Kucharik, C. J., Monfreda, C., Patz, J. A., Prentice, I. C., Ramankutty, N., and Snyder, P. K.: Global consequences of land use, *Science*, 309, 570-574, <https://doi.org/10.1126/science.1111772>, 2005.
- 780 Foody, G. M.: Sample size determination for image classification accuracy assessment and comparison, *International Journal of Remote Sensing*, 30, 5273-5291, <https://doi.org/10.1080/01431160903130937>, 2009.
- Foody, G. M. and Arora, M. K.: An evaluation of some factors affecting the accuracy of classification by an artificial neural network, *International Journal of Remote Sensing*, 18, 799-810, <https://doi.org/10.1080/014311697218764>, 2010.
- 785 Friedl, M. A., Sulla-Menashe, D., Tan, B., Schneider, A., Ramankutty, N., Sibley, A., and Huang, X.: MODIS Collection 5 global land cover: Algorithm refinements and characterization of new datasets, *Remote Sensing of Environment*, 114, 168-182, <https://doi.org/10.1016/j.rse.2009.08.016>, 2010.
- Friedl, M. A., Woodcock, C. E., Olofsson, P., Zhu, Z., Loveland, T., Stanimirova, R., Arevalo, P., Bullock, E., Hu, K.-T., Zhang, Y., Turlej, K., Tarrio, K., McAvoy, K., Gorelick, N., Wang, J. A., Barber, C. P., and Souza, C.: Medium Spatial Resolution Mapping of Global Land Cover and Land Cover Change Across Multiple
- 790 Decades From Landsat, *Frontiers in Remote Sensing*, 3, <https://doi.org/10.3389/frsen.2022.894571>, 2022.
- Friedlingstein, P., O'Sullivan, M., Jones, M. W., Andrew, R. M., Hauck, J., Olsen, A., Peters, G. P., Peters, W., Pongratz, J., Sitch, S., Le Quéré, C., Canadell, J. G., Ciais, P., Jackson, R. B., Alin, S., Aragão, L. E. O. C., Arneeth, A., Arora, V., Bates, N. R., Becker, M., Benoit-Cattin, A., Bittig, H. C., Bopp, L., Bultan, S., Chandra, N., Chevallier, F., Chini, L. P., Evans, W., Florentie, L., Forster, P. M., Gasser, T., Gehlen, M.,
- 795 Gilfillan, D., Gkritzalis, T., Gregor, L., Gruber, N., Harris, I., Hartung, K., Haverd, V., Houghton, R. A., Ilyina, T., Jain, A. K., Joetzjer, E., Kadono, K., Kato, E., Kitidis, V., Korsbakken, J. I., Landschützer, P., Lefèvre, N., Lenton, A., Lienert, S., Liu, Z., Lombardozzi, D., Marland, G., Metzl, N., Munro, D. R., Nabel, J. E. M. S., Nakaoka, S.-I., Niwa, Y., O'Brien, K., Ono, T., Palmer, P. I., Pierrot, D., Poulter, B., Resplandy, L.,

- Robertson, E., Rödenbeck, C., Schwinger, J., Séférian, R., Skjelvan, I., Smith, A. J. P., Sutton, A. J., Tanhua, T., Tans, P. P., Tian, H., Tilbrook, B., van der Werf, G., Vuichard, N., Walker, A. P., Wanninkhof, R., Watson, A. J., Willis, D., Wiltshire, A. J., Yuan, W., Yue, X., and Zaehle, S.: Global Carbon Budget 2020, *Earth Syst. Sci. Data*, 12, 3269-3340, <https://doi.org/10.5194/essd-12-3269-2020>, 2020.
- Gallant, A.: The Challenges of Remote Monitoring of Wetlands, *Remote Sensing*, 7, 10938-10950, <https://doi.org/10.3390/rs70810938>, 2015.
- Gao, Y., Liu, L., Zhang, X., Chen, X., Mi, J., and Xie, S.: Consistency Analysis and Accuracy Assessment of Three Global 30-m Land-Cover Products over the European Union using the LUCAS Dataset, *Remote Sensing*, 12, 3479, <https://doi.org/10.3390/rs12213479>, 2020.
- Ge, F., Xu, M., Gong, C., Zhang, Z., Tan, Q., and Pan, X.: Land cover changes the soil moisture response to rainfall on the Loess Plateau, *Hydrological Processes*, 36, <https://doi.org/10.1002/hyp.14714>, 2022.
- Giri, C., Pengra, B., Long, J., and Loveland, T. R.: Next generation of global land cover characterization, mapping, and monitoring, *International Journal of Applied Earth Observation and Geoinformation*, 25, 30-37, <https://doi.org/10.1016/j.jag.2013.03.005>, 2013.
- Gislason, P. O., Benediktsson, J. A., and Sveinsson, J. R.: Random Forests for land cover classification, *Pattern Recognition Letters*, 27, 294-300, <https://doi.org/10.1016/j.patrec.2005.08.011>, 2006.
- Gong, P., Li, X., and Zhang, W.: 40-Year (1978–2017) human settlement changes in China reflected by impervious surfaces from satellite remote sensing, *Science Bulletin*, 64, 756-763, <https://doi.org/10.1016/j.scib.2019.04.024>, 2019.
- Gorelick, N., Hancher, M., Dixon, M., Ilyushchenko, S., Thau, D., and Moore, R.: Google Earth Engine: Planetary-scale geospatial analysis for everyone, *Remote Sensing of Environment*, 202, 18-27, <https://doi.org/10.1016/j.rse.2017.06.031>, 2017.
- Hansen, M. C. and Loveland, T. R.: A review of large area monitoring of land cover change using Landsat data, *Remote Sensing of Environment*, 122, 66-74, <https://doi.org/10.1016/j.rse.2011.08.024>, 2012.
- Hansen, M. C., Potapov, P. V., Moore, R., Hancher, M., Turubanova, S. A., Tyukavina, A., Thau, D., Stehman, S. V., Goetz, S. J., Loveland, T. R., Kommareddy, A., Egorov, A., Chini, L., Justice, C. O., and Townshend, J. R.: High-resolution global maps of 21st-century forest cover change, *Science*, 342, 850-853, <https://doi.org/10.1126/science.1244693>, 2013.
- Harris, N. L., Gibbs, D. A., Baccini, A., Birdsey, R. A., de Bruin, S., Farina, M., Fatoyinbo, L., Hansen, M. C., Herold, M., Houghton, R. A., Potapov, P. V., Suarez, D. R., Roman-Cuesta, R. M., Saatchi, S. S., Slay, C. M., Turubanova, S. A., and Tyukavina, A.: Global maps of twenty-first century forest carbon fluxes, *Nature Climate Change*, 11, 234-240, <https://doi.org/10.1038/s41558-020-00976-6>, 2021.
- Healey, S. P., Cohen, W. B., Yang, Z., Kenneth Brewer, C., Brooks, E. B., Gorelick, N., Hernandez, A. J., Huang, C., Joseph Hughes, M., Kennedy, R. E., Loveland, T. R., Moisen, G. G., Schroeder, T. A., Stehman, S. V., Vogelmann, J. E., Woodcock, C. E., Yang, L., and Zhu, Z.: Mapping forest change using stacked generalization: An ensemble approach, *Remote Sensing of Environment*, 204, 717-728, <https://doi.org/10.1016/j.rse.2017.09.029>, 2018.
- Herold, M., Mayaux, P., Woodcock, C. E., Baccini, A., and Schmullius, C.: Some challenges in global land cover mapping: An assessment of agreement and accuracy in existing 1 km datasets, *Remote Sensing of Environment*, 112, 2538-2556, <https://doi.org/10.1016/j.rse.2007.11.013>, 2008.
- Homer, C., Dewitz, J., Jin, S., Xian, G., Costello, C., Danielson, P., Gass, L., Funk, M., Wickham, J., Stehman, S., Auch, R., and Riitters, K.: Conterminous United States land cover change patterns 2001–2016



- from the 2016 National Land Cover Database, *ISPRS Journal of Photogrammetry and Remote Sensing*, 162, 184-199, <https://doi.org/10.1016/j.isprsjprs.2020.02.019>, 2020.
- 845 Hong, C., Burney, J. A., Pongratz, J., Nabel, J., Mueller, N. D., Jackson, R. B., and Davis, S. J.: Global and regional drivers of land-use emissions in 1961-2017, *Nature*, 589, 554-561, <https://doi.org/10.1038/s41586-020-03138-y>, 2021.
- Huang, C., Goward, S. N., Schleeweis, K., Thomas, N., Masek, J. G., and Zhu, Z.: Dynamics of national forests assessed using the Landsat record: Case studies in eastern United States, *Remote Sensing of Environment*, 113, 1430-1442, <https://doi.org/10.1016/j.rse.2008.06.016>, 2009.
- 850 Jin, H., Stehman, S. V., and Mountrakis, G.: Assessing the impact of training sample selection on accuracy of an urban classification: a case study in Denver, Colorado, *International Journal of Remote Sensing*, 35, 2067-2081, <https://doi.org/10.1080/01431161.2014.885152>, 2014.
- Jin, S., Dewitz, J., Li, C., Sorenson, D., Zhu, Z., Shogib, M. R. I., Danielson, P., Granneman, B., Costello, C., Case, A., and Gass, L.: National Land Cover Database 2019: A Comprehensive Strategy for Creating the 1986–2019 Forest Disturbance Product, *Journal of Remote Sensing*, 3, 855 <https://doi.org/10.34133/remotesensing.0021>, 2023.
- Jin, S., Yang, L., Zhu, Z., and Homer, C.: A land cover change detection and classification protocol for updating Alaska NLCD 2001 to 2011, *Remote Sensing of Environment*, 195, 44-55, <https://doi.org/10.1016/j.rse.2017.04.021>, 2017.
- 860 Kennedy, R. E., Cohen, W. B., and Schroeder, T. A.: Trajectory-based change detection for automated characterization of forest disturbance dynamics, *Remote Sensing of Environment*, 110, 370-386, <https://doi.org/10.1016/j.rse.2007.03.010>, 2007.
- Kennedy, R. E., Yang, Z., and Cohen, W. B.: Detecting trends in forest disturbance and recovery using yearly Landsat time series: 1. LandTrendr — Temporal segmentation algorithms, *Remote Sensing of Environment*, 114, 2897-2910, <https://doi.org/10.1016/j.rse.2010.07.008>, 2010.
- 865 Kenny, Q. Y.: Indicator function and its application in two-level factorial designs, *The Annals of Statistics*, 31, 984-994, <https://doi.org/10.1214/aos/1056562470>, 2003.
- Li, X., Gong, P., and Liang, L.: A 30-year (1984–2013) record of annual urban dynamics of Beijing City derived from Landsat data, *Remote Sensing of Environment*, 166, 78-90, <https://doi.org/10.1016/j.rse.2015.06.007>, 2015.
- 870 Liu, C., Zhang, Q., Luo, H., Qi, S., Tao, S., Xu, H., and Yao, Y.: An efficient approach to capture continuous impervious surface dynamics using spatial-temporal rules and dense Landsat time series stacks, *Remote Sensing of Environment*, 229, 114-132, <https://doi.org/10.1016/j.rse.2019.04.025>, 2019.
- Liu, H., Gong, P., Wang, J., Wang, X., Ning, G., and Xu, B.: Production of global daily seamless data cubes and quantification of global land cover change from 1985 to 2020 - iMap World 1.0, *Remote Sensing of Environment*, 258, 112364, <https://doi.org/10.1016/j.rse.2021.112364>, 2021a.
- 875 Liu, L., Zhang, X., Chen, X., Gao, Y., and Mi, J.: GLC\_FCS30-2020: Global Land Cover with Fine Classification System at 30m in 2020 (v1.2), Zenodo [data]. 2020.
- Liu, L., Zhang, X., Gao, Y., Chen, X., Shuai, X., and Mi, J.: Finer-Resolution Mapping of Global Land Cover: Recent Developments, Consistency Analysis, and Prospects, *Journal of Remote Sensing*, 2021, 5289697, 880 <https://doi.org/10.34133/2021/5289697>, 2021b.
- Liu, L., Zhang, X., and Zhao, T.: GLC\_FCS30D: the first global 30-m land-cover dynamic monitoring product with fine classification system from 1985 to 2022, Zenodo [data set]. 2023.

- Millard, K. and Richardson, M.: On the Importance of Training Data Sample Selection in Random Forest Image Classification: A Case Study in Peatland Ecosystem Mapping, *Remote Sensing*, 7, 8489-8515, <https://doi.org/10.3390/rs70708489>, 2015.
- 885 Pekel, J. F., Cottam, A., Gorelick, N., and Belward, A. S.: High-resolution mapping of global surface water and its long-term changes, *Nature*, 540, 418-422, <https://doi.org/10.1038/nature20584>, 2016.
- Pengra, B., Gallant, A., Zhu, Z., and Dahal, D.: Evaluation of the Initial Thematic Output from a Continuous Change-Detection Algorithm for Use in Automated Operational Land-Change Mapping by the U.S. Geological Survey, *Remote Sensing*, 8, 811, <https://doi.org/10.3390/rs8100811>, 2016.
- 890 Pontus Olofsson, G. M. F.: Good practices for estimating area and assessing accuracy of land change, *Remote Sensing of Environment*, 148, 42-57, <https://doi.org/10.1016/j.rse.2014.02.015>, 2014.
- Potapov, P., Hansen, M. C., Pickens, A., Hernandez-Serna, A., Tyukavina, A., Turubanova, S., Zalles, V., Li, X., Khan, A., Stolle, F., Harris, N., Song, X.-P., Baggett, A., Kommareddy, I., and Kommareddy, A.: The 895 Global 2000-2020 Land Cover and Land Use Change Dataset Derived From the Landsat Archive: First Results, *Frontiers in Remote Sensing*, 3, <https://doi.org/10.3389/frsen.2022.856903>, 2022.
- Potapov, P., Turubanova, S., Hansen, M. C., Tyukavina, A., Zalles, V., Khan, A., Song, X.-P., Pickens, A., Shen, Q., and Cortez, J.: Global maps of cropland extent and change show accelerated cropland expansion in the twenty-first century, *Nature Food*, 3, 19-28, <https://doi.org/10.1038/s43016-021-00429-z>, 2021.
- 900 Qin, Y., Xiao, X., Wigneron, J.-P., Ciais, P., Canadell, J. G., Brandt, M., Li, X., Fan, L., Wu, X., Tang, H., Dubayah, R., Doughty, R., Chang, Q., Crowell, S., Zheng, B., Neal, K., Celis, J. A., and Moore, B.: Annual Maps of Forests in Australia from Analyses of Microwave and Optical Images with FAO Forest Definition, *Journal of Remote Sensing*, 2021, <https://doi.org/10.34133/2021/9784657>, 2021.
- Radoux, J., Lamarche, C., Van Bogaert, E., Bontemps, S., Brockmann, C., and Defourny, P.: Automated 905 Training Sample Extraction for Global Land Cover Mapping, *Remote Sensing*, 6, 3965-3987, <https://doi.org/10.3390/rs6053965>, 2014.
- Roy, D. P., Kovalskyy, V., Zhang, H. K., Vermote, E. F., Yan, L., Kumar, S. S., and Egorov, A.: Characterization of Landsat-7 to Landsat-8 reflective wavelength and normalized difference vegetation index continuity, *Remote Sensing of Environment*, 185, 57-70, <https://doi.org/10.1016/j.rse.2015.12.024>, 2016.
- 910 Roy, D. P., Qin, Y., Kovalskyy, V., Vermote, E. F., Ju, J., Egorov, A., Hansen, M. C., Kommareddy, I., and Yan, L.: Conterminous United States demonstration and characterization of MODIS-based Landsat ETM+ atmospheric correction, *Remote Sensing of Environment*, 140, 433-449, <https://doi.org/10.1016/j.rse.2013.09.012>, 2014a.
- Roy, D. P., Wulder, M. A., Loveland, T. R., C.E. W., Allen, R. G., Anderson, M. C., Helder, D., Irons, J. R., 915 Johnson, D. M., Kennedy, R., Scambos, T. A., Schaaf, C. B., Schott, J. R., Sheng, Y., Vermote, E. F., Belward, A. S., Bindschadler, R., Cohen, W. B., Gao, F., Hipple, J. D., Hostert, P., Huntington, J., Justice, C. O., Kilic, A., Kovalskyy, V., Lee, Z. P., Lymburner, L., Masek, J. G., McCorkel, J., Shuai, Y., Trezza, R., Vogelmann, J., Wynne, R. H., and Zhu, Z.: Landsat-8: Science and product vision for terrestrial global change research, *Remote Sensing of Environment*, 145, 154-172, <https://doi.org/10.1016/j.rse.2014.02.001>, 2014b.
- 920 Song, X. P., Hansen, M. C., Stehman, S. V., Potapov, P. V., Tyukavina, A., Vermote, E. F., and Townshend, J. R.: Global land change from 1982 to 2016, *Nature*, 560, 639-643, <https://doi.org/10.1038/s41586-018-0411-9>, 2018.
- Stehman, S. V., Pengra, B. W., Horton, J. A., and Wellington, D. F.: Validation of the U.S. Geological Survey's Land Change Monitoring, Assessment and Projection (LCMAP) Collection 1.0 annual land cover

- 925 products 1985–2017, *Remote Sensing of Environment*, 265, 112646, <https://doi.org/10.1016/j.rse.2021.112646>, 2021.
- Sulla-Menashe, D., Gray, J. M., Abercrombie, S. P., and Friedl, M. A.: Hierarchical mapping of annual global land cover 2001 to present: The MODIS Collection 6 Land Cover product, *Remote Sensing of Environment*, 222, 183-194, <https://doi.org/10.1016/j.rse.2018.12.013>, 2019.
- 930 Tachikawa, T., Hato, M., Kaku, M., and Iwasaki, A.: Characteristics of ASTER GDEM Version 2, *Geoscience and Remote Sensing Symposium (IGARSS)*, doi: 10.1109/IGARSS.2011.6050017, 2011. 3657-3660, <https://doi.org/10.1109/IGARSS.2011.6050017>, 2011.
- Venter, Z. S., Barton, D. N., Chakraborty, T., Simensen, T., and Singh, G.: Global 10 m Land Use Land Cover Datasets: A Comparison of Dynamic World, World Cover and Esri Land Cover, *Remote Sensing*, 14, 4101, <https://doi.org/10.3390/rs14164101>, 2022.
- 935 Verbesselt, J., Hyndman, R., Newnham, G., and Culvenor, D.: Detecting trend and seasonal changes in satellite image time series, *Remote sensing of Environment*, 114, 106-115, 2010.
- Vermote, E.: LEDAPS surface reflectance product description, 2007. 2007.
- Vermote, E. F. and Kotchenova, S.: Atmospheric correction for the monitoring of land surfaces, *Journal of Geophysical Research*, 113, <https://doi.org/10.1029/2007jd009662>, 2008.
- 940 Wang, N., Zhang, X., Yao, S., Wu, J., and Xia, H.: How Good Are Global Layers for Mapping Rural Settlements? Evidence from China, *Land*, 11, 1308, <https://doi.org/10.3390/land11081308>, 2022.
- Winkler, K., Fuchs, R., Rounsevell, M., and Herold, M.: Global land use changes are four times greater than previously estimated, *Nat Commun*, 12, 2501, <https://doi.org/10.1038/s41467-021-22702-2>, 2021.
- 945 Xian, G. Z., Smith, K., Wellington, D., Horton, J., Zhou, Q., Li, C., Auch, R., Brown, J. F., Zhu, Z., and Reker, R. R.: Implementation of the CCDC algorithm to produce the LCMAP Collection 1.0 annual land surface change product, *Earth Syst. Sci. Data*, 14, 143-162, <https://doi.org/10.5194/essd-14-143-2022>, 2022.
- Xiao, Y., Wang, Q., Tong, X., and Atkinson, P. M.: Thirty-meter map of young forest age in China, *Earth Syst. Sci. Data*, 15, 3365-3386, <https://doi.org/10.5194/essd-15-3365-2023>, 2023.
- 950 Xie, S., Liu, L., Zhang, X., and Yang, J.: Mapping the annual dynamics of land cover in Beijing from 2001 to 2020 using Landsat dense time series stack, *ISPRS Journal of Photogrammetry and Remote Sensing*, 185, 201-218, <https://doi.org/10.1016/j.isprsjprs.2022.01.014>, 2022.
- Yang, J. and Huang, X.: The 30 m annual land cover dataset and its dynamics in China from 1990 to 2019, *Earth Syst. Sci. Data*, 13, 3907-3925, <https://doi.org/10.5194/essd-13-3907-2021>, 2021.
- 955 Ye, S., Rogan, J., Zhu, Z., and Eastman, J. R.: A near-real-time approach for monitoring forest disturbance using Landsat time series: stochastic continuous change detection, *Remote Sensing of Environment*, 252, 112167, <https://doi.org/10.1016/j.rse.2020.112167>, 2021.
- Zhang, H. K. and Roy, D. P.: Using the 500 m MODIS land cover product to derive a consistent continental scale 30 m Landsat land cover classification, *Remote Sensing of Environment*, 197, 15-34, <https://doi.org/10.1016/j.rse.2017.05.024>, 2017.
- 960 Zhang, X., Liu, L., Chen, X., Gao, Y., and Jiang, M.: Automatically Monitoring Impervious Surfaces Using Spectral Generalization and Time Series Landsat Imagery from 1985 to 2020 in the Yangtze River Delta, *Journal of Remote Sensing*, 2021, 1-16, <https://doi.org/10.34133/2021/9873816>, 2021a.
- Zhang, X., Liu, L., Chen, X., Gao, Y., Xie, S., and Mi, J.: GLC\_FCS30: global land-cover product with fine classification system at 30 m using time-series Landsat imagery, *Earth Syst. Sci. Data*, 13, 2753-2776, <https://doi.org/10.5194/essd-13-2753-2021>, 2021b.
- 965

- Zhang, X., Liu, L., Chen, X., Xie, S., and Gao, Y.: Fine Land-Cover Mapping in China Using Landsat Datacube and an Operational SPECLib-Based Approach, *Remote Sensing*, 11, 1056, <https://doi.org/10.3390/rs11091056>, 2019.
- 970 Zhang, X., Liu, L., Wu, C., Chen, X., Gao, Y., Xie, S., and Zhang, B.: Development of a global 30 m impervious surface map using multisource and multitemporal remote sensing datasets with the Google Earth Engine platform, *Earth Syst. Sci. Data*, 12, 1625-1648, <https://doi.org/10.5194/essd-12-1625-2020>, 2020.
- Zhang, X., Liu, L., Zhao, T., Chen, X., Lin, S., Wang, J., Mi, J., and Liu, W.: GWL\_FCS30: a global 30 m wetland map with a fine classification system using multi-sourced and time-series remote sensing imagery in 975 2020, *Earth Syst. Sci. Data*, 15, 265-293, <https://doi.org/10.5194/essd-15-265-2023>, 2023.
- Zhang, X., Liu, L., Zhao, T., Gao, Y., Chen, X., and Mi, J.: GISD30: global 30 m impervious-surface dynamic dataset from 1985 to 2020 using time-series Landsat imagery on the Google Earth Engine platform, *Earth Syst. Sci. Data*, 14, 1831-1856, <https://doi.org/10.5194/essd-14-1831-2022>, 2022.
- Zhang, Y., Ling, F., Wang, X., Foody, G. M., Boyd, D. S., Li, X., Du, Y., and Atkinson, P. M.: Tracking 980 small-scale tropical forest disturbances: Fusing the Landsat and Sentinel-2 data record, *Remote Sensing of Environment*, 261, 112470, <https://doi.org/10.1016/j.rse.2021.112470>, 2021c.
- Zhao, T., Zhang, X., Gao, Y., Mi, J., Liu, W., Wang, J., Jiang, M., and Liu, L.: Assessing the Accuracy and Consistency of Six Fine-Resolution Global Land Cover Products Using a Novel Stratified Random Sampling Validation Dataset, *Remote Sensing*, 15, 2285, 2023.
- 985 Zhu, Z.: Change detection using landsat time series: A review of frequencies, preprocessing, algorithms, and applications, *ISPRS Journal of Photogrammetry and Remote Sensing*, 130, 370-384, <https://doi.org/10.1016/j.isprsjprs.2017.06.013>, 2017.
- Zhu, Z., Gallant, A. L., Woodcock, C. E., Pengra, B., Olofsson, P., Loveland, T. R., Jin, S., Dahal, D., Yang, L., and Auch, R. F.: Optimizing selection of training and auxiliary data for operational land cover 990 classification for the LCMAP initiative, *ISPRS Journal of Photogrammetry and Remote Sensing*, 122, 206-221, <https://doi.org/10.1016/j.isprsjprs.2016.11.004>, 2016.
- Zhu, Z., Wang, S. X., and Woodcock, C. E.: Improvement and expansion of the Fmask algorithm: cloud, cloud shadow, and snow detection for Landsats 4-7, 8, and Sentinel 2 images, *Remote Sensing of Environment*, 159, 269-277, <https://doi.org/10.1016/j.rse.2014.12.014>, 2015.
- 995 Zhu, Z. and Woodcock, C. E.: Automated cloud, cloud shadow, and snow detection in multitemporal Landsat data: An algorithm designed specifically for monitoring land cover change, *Remote Sensing of Environment*, 152, 217-234, <https://doi.org/10.1016/j.rse.2014.06.012>, 2014a.
- Zhu, Z. and Woodcock, C. E.: Continuous change detection and classification of land cover using all available Landsat data, *Remote Sensing of Environment*, 144, 152-171, <https://doi.org/10.1016/j.rse.2014.01.011>, 1000 2014b.
- Zhu, Z. and Woodcock, C. E.: Object-based cloud and cloud shadow detection in Landsat imagery, *Remote Sensing of Environment*, 118, 83-94, <https://doi.org/10.1016/j.rse.2011.10.028>, 2012.
- Zhu, Z., Woodcock, C. E., and Olofsson, P.: Continuous monitoring of forest disturbance using all available Landsat imagery, *Remote Sensing of Environment*, 122, 75-91, <https://doi.org/10.1016/j.rse.2011.10.030>, 1005 2012.
- Zhu, Z., Zhang, J., Yang, Z., Aljaddani, A. H., Cohen, W. B., Qiu, S., and Zhou, C.: Continuous monitoring of land disturbance based on Landsat time series, *Remote Sensing of Environment*, doi: 10.1016/j.rse.2019.03.009, 2019. <https://doi.org/10.1016/j.rse.2019.03.009>, 2019.

